universe

MDPI

Article

Comparative Role of $^{14}C(n,\gamma)^{15}C$ and $^{14}C(p,\gamma)^{15}N$ Reactions in the Production of ^{15}N: Maxwell–Boltzmann and Tsallis Frameworks

Alessya S. Tkachenko [1,*], Nataliya A. Burkova [2], Roman Ya. Kezerashvili [3,4], Badigul M. Yeleusheva [1], Bekmurza B. Beisenov [2] and Sergey B. Dubovichenko [1,*]

1 Department of Science, META University, Almaty 050000, Kazakhstan; eleusheva.badigul@gmail.com
2 Department of Theoretical and Nuclear Physics, Al-Farabi Kazakh National University, Almaty 050040, Kazakhstan; natali.burkova@gmail.com (N.A.B.); bekmurza.beisenov@gmail.com (B.B.B.)
3 New York City College of Technology, City University of New York, Brooklyn, NY 11201, USA; rkezerashvili@citytech.cuny.edu
4 Graduate School and University Center, City University of New York, New York, NY 10016, USA
* Correspondence: tkachenko.alessya@gmail.com (A.S.T.); dubovichenko@mail.ru (S.B.D.)

Abstract

The radiative capture reactions $^{14}C(n,\gamma_{0+1})^{15}C$ and $^{14}C(p,\gamma_0)^{15}N$ are investigated within a framework of the modified potential cluster model. A comprehensive review of recent experimental and theoretical studies of the $^{14}C(n,\gamma)^{15}C$ reaction is presented, including comparisons with ANC-based approaches and recent ab initio calculations. For the $^{14}C(p,\gamma_0)^{15}N$ reaction, elastic scattering phase shifts, interaction potentials, total cross-sections, astrophysical S-factors, and reaction rates are calculated up to $E_{c.m.} = 5$ MeV. The analysis includes two resonances at $1/2^+$ ($^2S_{1/2}$) at $E_x = 11.615(4)$ MeV and $3/2^+$ ($^2D_{3/2}$) at $E_x = 13.390(10)$ MeV. The zero-energy astrophysical S-factor is estimated as $S(0) \approx 4.5(1)$ keV·b. Reaction rates for both capture processes are calculated over the temperature range $T_9 = 0.01$–10 within the Maxwell–Boltzmann and non-extensive Tsallis statistical frameworks. A phenomenological sensitivity analysis based on Tsallis statistics is performed to investigate how assumed deviations from Maxwell–Boltzmann energy distributions modify the neutron and proton capture reaction rates and their cross-over temperatures. Numerical results reveal a new relationship between neutron and proton capture at Asymptotic Giant Branch stars shell temperatures $T_9 \approx 0.02$–0.15, relevant to ^{15}N production in neutron-rich environments.

Keywords: low and astrophysical energies; $n^{14}C$ and $p^{14}C$ systems; radiative capture; thermonuclear reaction rate; potential cluster model; Tsallis statistics

Check for updates

Academic Editors: Máté Csanád and Sergio Cristallo

Received: 20 July 2026
Revised: 16 October 2026
Accepted: 3 November 2026
Published: 9 November 2026

Copyright: © 2026 by the authors. Licensee MDPI, Basel, Switzerland. This article is an open access article distributed under the terms and conditions of the Creative Commons Attribution (CC BY) license.

1. Introduction

Data on the radiative capture reaction rates of protons (p,γ) and neutrons (n,γ) allow us to test the hypothesis of primordial nucleosynthesis in an inhomogeneous Universe [1–4]. This model assumes that following the Big Bang, the Universe underwent stratification into regions with different concentrations of protons n_p and neutrons n_n. This picture differs from the standard homogeneous cosmological model, in which baryons are uniformly distributed, and their velocities follow the Maxwell–Boltzmann distribution. In neutron-rich regions, neutron capture reactions may significantly alter the abundances of light- and intermediate-mass nuclei produced during Big Bang nucleosynthesis (BBN), leading to nucleosynthesis pathways different from those dominated by proton-induced reactions.

Primordial nucleosynthesis ends with the formation of stable ^{7}Li, after which various chains of synthesis of elements with A > 7 begin to form in thermonuclear reactions involving protons, neutrons, and α-particles [5]. Radiative proton and neutron capture reactions govern the production of heavier elements, the composition and concentration of which in stellar objects are observable quantities. Consequently, reliable information about the composition of heavy nuclei makes it possible to follow the evolution of a star, starting from the mechanisms of light elements formation.

Another example of stellar conditions where the competing role of (p,γ) and (n,γ) reactions may play a significant role is the *carbon pocket* structure of the Asymptotic Giant Branch (AGB) stars [6,7]. The proton density n_p of stellar plasma initially exceeds the neutron density n_n. However, the carbon pockets may experience short-time injections from the neighboring zones, and their density temperature (ρT state) may lead to an increase in neutron concentration. Thermal pulses may also lead to deviations of the proton and neutron velocity distributions from their equilibrium forms. This phenomenon could be taken into account by applying the non-extensive Tsallis statistics proposed in [8] and tested for the primordial BBN in [5,9–11]. In the present work, we employ non-extensive Tsallis statistics to investigate the radiative proton and neutron capture reactions on the carbon isotope ^{14}C.

One of the key tasks of nuclear astrophysics is to *reconstruct* the sequence of synthesis of chemical elements in thermonuclear processes, considering the most probable branching of such chains. This probability depends on a number of factors:

1. The density of the combustible components, namely neutrons and protons at a given temperature of the stellar environment;
2. The density of accumulated nuclei of chain constituents for a given atomic number Z;
3. The rates of radiative capture reactions (p,γ) and (n,γ), which govern the different scenarios of chain evolution, but both of which may lead to the synthesis of a new element with Z + 1 either directly or via β-decay.

The present study addresses the third factor by investigating the radiative capture reactions ^{14}C$(n,\gamma)^{15}$C$(\beta^-)^{15}$N and ^{14}C$(p,\gamma)^{15}$N, both of which lead to the formation of nitrogen isotope ^{15}N via ^{14}C as a seed nucleus. The ^{14}C isotope is special—its lifetime is more than 5000 years, i.e., it is an unstable but long-lived isotope. ^{14}C is not included in the standard CNO hydrogen combustion cycles [12]. At the same time, the reactions ^{14}C$(n,\gamma)^{15}$C and ^{14}C$(p,\gamma)^{15}$N are included in the general network for calculating the mass fraction of elements produced by nucleosynthesis, starting from primordial and up to CNO and H-CNO cycles [13].

In the context of the first factor, the neutron and proton densities in certain regions of AGB stars may become sufficiently comparable for both neutron capture and proton capture reaction pathways to compete. Today, the estimations of neutron densities lead to the values $n_n = 10^{15}$–10^{17} cm^{-3} (see [14] and references therein). These conditions give a reasonable background for the earlier models of the *neutron-induced* CNO cycles, which cover the stellar evolution of AGB stars via the *intermediate* processes (*i*-processes). The carbon chain was suggested more than 30 years ago by Kajino [15]

$$^{12}\mathrm{C}(n,\gamma)^{13}\mathrm{C}(n,\gamma)\underline{^{\mathbf{14}}\mathbf{C}(n,\gamma)^{15}\mathrm{C}}(\beta^-)^{\mathbf{15}}\mathbf{N}(n,\gamma)^{16}\mathrm{N}(\beta^-)^{16}\mathrm{O}(n,^{4}\mathrm{He})^{\mathbf{14}}\mathbf{C}\ldots, \quad (1)$$

and they found a more detailed interpretation later in Refs. [15–18]. The experimental study of the total cross-section of reaction ^{14}C$(n,\gamma)^{15}$C is currently provided by five datasets [19–23], which match each other more qualitatively than quantitatively. Therefore, theoretical calculations are the way to find the mutually confirmed predictions for the reaction rate of the ^{14}C$(n,\gamma)^{15}$C process.

The refinement and expansion of nuclear reaction networks contribute directly to a more accurate determination of the abundances of seed nuclei discussed in the second factor.

In this work, we present the comparative summary of our results on the cross-sections and reaction rates of $^{14}C(n,\gamma)^{15}C$ obtained by our detailed calculations [24] in the framework of the modified potential cluster model (MPCM), along with recent calculations by Jiang et al. [25] and ab initio results by Navratil et al. [26]. Additional reference calculations by Ma et al. [27] and Bhattacharyya et al. [28] are also included in the comparison.

Other sources of stellar ^{15}N isotope are the *proton-induced* CNO cycles.

$$\begin{array}{ll} \text{(I)} & {}^{12}C(p,\gamma)^{13}N(\beta^+)^{13}C(p,\gamma)^{14}N(p,\gamma)^{15}O(\beta^+)\mathbf{^{15}N}(p,\alpha)^{12}C, \\ & \qquad\qquad\qquad\qquad\qquad\qquad\qquad\qquad\qquad\qquad \downarrow \\ \text{(II)} & \qquad\qquad\qquad\qquad\qquad\qquad\qquad\qquad\qquad\qquad \mathbf{^{15}N}(p,\gamma)^{16}O(p,\gamma)^{17}F(\beta^+)^{17}O(p,\alpha)^{14}N(p,\gamma)^{15}O(\beta^+)\mathbf{^{15}N}(p,\alpha)^{12}C \end{array} \quad (2)$$

The dominant sequence in the Sun is sequence (I) [13]. In addition to the reactions in chains (1) and (2), the production of the isotope ^{15}N can also occur through the direct combustion of hydrogen on carbon ^{14}C, namely through the reaction $^{14}C(p,\gamma)^{15}N$. Note that, for this reaction, there is only one set of measured cross-sections in the energy range $E_{c.m.}$ ~ 250–700 keV [29]. The scarcity of experimental data limits the reliability of an *R*-matrix analysis and increases the uncertainty of extrapolations to astrophysically relevant energies. Consequently, other theoretical approaches are required to obtain more robust predictions of the reaction cross-section and reaction rate.

We applied the MPCM for the calculation of the cross-section of $^{14}C(p,\gamma_0)^{15}N$ reaction, low-energy astrophysical *S*-factor, and corresponding reaction rate. Next, the primary emphasis is on comparing the present results for the reaction rate with those obtained by Iliadis et al. using the statistical Monte Carlo approach [30,31].

The primary objective of the present study is twofold. First, we calculate the reaction rate of the radiative proton capture reaction on ^{14}C isotope. Second, we use the obtained rates of $^{14}C(n,\gamma)^{15}C$ and $^{14}C(p,\gamma)^{15}N$ reactions to determine the energy and temperature ranges T_9 ($T_9 = 10^9$ K) where transition from the neutron channel to the proton channel may occur.

Earlier, the comparison of $^{14}C(n,\gamma)^{15}C$ and $^{14}C(p,\gamma)^{15}N$ reaction rates has been proposed by Wiescher et al. (1990) [32] for the evaluation of the nonstandard BBN production of CNO elements. This issue was developed by Kawano et al. (1991) and was supplemented by the calculation of the mass fraction of light elements for various baryon density conditions [33]. A compilation on the relative temperature dependence of the $^{14}C(n,\gamma)^{15}C$ and $^{14}C(p,\gamma)^{15}N$ reaction rates is presented in 2014 by Shubhchintak et al.in Ref. [34].

We consider questionable the conclusions of Refs [32–34] on the temperature range where the $^{14}C(n,\gamma)^{15}C$ reaction will dominate over $^{14}C(p,\gamma)^{15}N$ as they are based on reaction rates obtained by different methods (see Section 5 for details).

In contrast, the present study provides a consistent determination of the ratio between the (n,γ) and (p,γ) reaction rates on ^{14}C since both reactions were analyzed within the same MPCM approach.

The present investigation extends our previous study of the $^{14}C(n,\gamma)^{15}C$ reaction [24] by examining the $^{14}C(p,\gamma)^{15}N$ process within the same modified potential cluster model framework. While the neutron capture results established in Ref. [24] provide the reference input, the principal focus of the present work is the calculation of proton capture cross-sections, astrophysical *S*-factors, and reaction rates, together with a systematic comparison of the two reaction pathways. Particular attention is devoted to the influence of non-extensive Tsallis statistics on their temperature-dependent reaction rates and on the conditions under which either capture process becomes dominant.

The rest of this paper is organized as follows: A brief description of the calculation method is presented in Section 2. A summary of the current status of $^{14}C(n,\gamma)^{15}C$ reaction is given in Section 3. Section 4 provides results for the $^{14}C(p,\gamma)^{15}N$ channel—classification of orbital states and interaction potentials, cross-sections, astrophysical *S*-factor, and Maxwell–Boltzmann reaction rates. A comparison of $^{14}C(n,\gamma)^{15}C$ and $^{14}C(p,\gamma)^{15}N$ reaction rates in Maxwell–Boltzmann and Tsallis statistics is presented in Section 5. The physical constraints, state dependence, and predictive character of the MPCM are presented in Section 6. Concluding remarks follow in Section 7.

2. Calculation Methods

The potential cluster model accounting the Pauli exclusion principle via the classification of the orbital states in the single-defined channel by the Young diagrams has been successfully applied to the series of radiative capture reactions relevant to the astrophysical energies [35,36]. Such a classification of the *allowed* and *forbidden* states determines initially the choice of the optimal depth for the inter-cluster interaction potential. Both shallow and deep potentials may lead to the same channel binding energy, but difference in nodal or nodeless radial wave functions behavior will reveal immediately the correctness of accounting the Pauli exclusion principle. The microscopic justification of the MPCM approach is provided in Refs. [37,38].

The basic framework of the MPCM can be summarized as follows [39]:

1. *Cluster representation and Pauli principle.* Nuclear states are classified according to Young orbital diagrams. This classification identifies allowed and forbidden states in individual partial waves and provides an effective implementation of the Pauli exclusion principle. The forbidden states determine the nodal structure of the radial wave functions of the physically allowed states.
2. *Intercluster interaction.* For each partial wave characterized by the corresponding quantum numbers, the nuclear interaction between the clusters is described by a Gaussian potential supplemented, when appropriate, by the Coulomb interaction. The potential parameters are chosen consistently with the number of forbidden states determined from the Young diagram classification.
3. *Bound-state potentials.* The potentials describing bound states are constrained by the experimental binding energies and asymptotic normalizing coefficients (ANCs). Their parameters may be varied within the experimental uncertainties of these quantities.
4. *Scattering state potentials.* The interaction potentials in the continuum are constrained by available elastic scattering phase shifts and by the energies and widths of resonant or excited states of the compound nucleus. In this way, the same cluster description provides the wave functions of both the initial scattering state and the final bound state.
5. *Wave functions and radiative capture.* The radial wave functions of the allowed discrete and continuum states are obtained with the correct asymptotic behavior. These wave functions are then used to evaluate the radial matrix elements of the *E*J and *M*J electromagnetic transitions and, consequently, the radiative capture cross-sections, astrophysical *S*-factors, and thermonuclear reaction rates.

Let us specify the main points how the MPCM method is implemented in our particular case.

1. The interaction potential of the specified partial state with the quantum numbers *JLS* is the two-parameter Gauss's form potential

$$V(r, JLS) = -V_0(JLS)\exp\{-\alpha(JLS)r^2\}, \quad (3)$$

where V_0 is the potential depth, and α is a parameter defining the asymptotic decrease of the potential at far-long relative distances r.

2. Constraints of the *bound state's* potential parameters V_0 and α are defined by the accuracy of the reproducing the channel binding energy E_b. An additional condition concerns the asymptotic behavior of the radial wave functions obtained as the solution of the Schrodinger equation, which should match the analytical Whittaker functions $W_{-\eta L+1/2}(2k_0 r)$ multiplied by the constant C at long distances, where $V(r, JLS) \to 0$:

$$\chi_L(r) = CW_{-\eta L+1/2}(2k_0 r), \text{ where } k_0 = \sqrt{2\mu E_b}/\hbar \quad (4)$$

Constant C is related to the experimentally available asymptotic normalizing coefficient as $A_{NC}^2 = S_F \cdot C^2$ via the spectroscopic factor S_F, which defines the purity of the single-cluster channel. Data on the ANC and S_F are the input information for the evaluation of the dimensionless constant $C_w = A_{NC}/\sqrt{2k_0 S_f}$, which appears naturally in the solution of the radial Schrodinger equation [39,40].

Once the binding energy E_b, which matches the experimentally obtained value, is determined, the process of adjusting the parameters V_0 and α continues until an appropriate value of C_w is identified. Additional check of the radial functions of the bound states suggests a comparison of calculated charge R_{ch}, and matter R_m radii with the experimental data.

3. Parameters V_0 and α for the *scattering wave functions* may be reliably determined if the data on the elastic scattering phase shifts are available either experimentally or provided by microscopic modal calculations. In the absence of phase shift data, the fitting of V_0 and α parameters is done using the experimentally determined resonance energies E_{res} and level's width Γ, for example [41,42].

The scattering radial wave function $\chi_i(r)$ is normalized to the asymptotics at the edge of the 50 fm interval, denoted as R

$$\chi_{JLS}(r \to R) \to \cos(\delta_{S,L}^J) F_L(kr) + \sin(\delta_{S,L}^J) G_L(kr) \quad (5)$$

where $F_L(kr)$ and $G_L(kr)$ are the regular and irregular Coulomb functions and $\delta_{S,L}^J$ are the scattering phase shifts. Relation (5) provides the calculation of phase shifts at two matching points [40].

Details of the MPCM formalism, construction of the interaction potentials, and computing procedure providing the calculation of radial matrix elements of EJ transitions $I_{EJ}(k,J_f,J_i) = (<\chi_f|r^J|\chi_i>)$ and MJ transitions $I_{MJ}(k,J_f,J_i) = (<\chi_f|r^{J-1}|\chi_i>)$, radiative capture cross-sections $\sigma(NJ,J_f)$, and astrophysical S-factors, can be found in Refs. [36,39,40,43,44]. The input data for the current calculations are provided in Appendix A.

3. ^{14}C(n,γ)^{15}C Reaction Status for the Comparative Analysis

Our recent paper [24] presents a detailed study of the ^{14}C(n,γ)^{15}C reaction within the framework of the MPCM approach and covers the results for the cross-section and reaction rates. Here, we briefly summarize the main findings of Ref. [24] and complement them with recent developments reported during 2025–2026.

3.1. Adopted Neutron Capture $^{14}C(n,\gamma)^{15}C$ Description

Radiative neutron capture proceeds predominantly via the electric dipole $E1$ transition to the ground state (GS, $J_f^\pi = 1/2^+$) and first excited state (1st ES, $5/2^+$) of ^{15}C via the $^2P_{1/2}$+$^2P_{3/2} \to {}^2S_{1/2}$ and $^2P_{3/2} \to {}^2D_{5/2}$ amplitudes, respectively.

The compiled ANCs, spectroscopic factors S_f, and asymptotic constants C_w are given in Table 1. The ANC values agree within 10–15% for the $^2S_{1/2}$ state, whereas the $^2D_{5/2}$ state shows greater variation. The partial capture cross-section to the 1st ES contributes ~5% relative to GS capture.

Table 1. ANC and asymptotic constant C_w data for the ^{15}C in the n^{14}C channel.

^{15}C(1/2$^+$) $^2S_{1/2}$-State, $\sqrt{2k_0} = 0.686$ fm$^{-1/2}$	ANC, fm$^{-1/2}$	S_f	C_w
McCleskey et al., 2014 [45]	1.37(7)	1	2.00(10)
Moschini et al., 2019 [46]	1.26(2)	1	1.84(3)
Ma et al., 2020 [27]	1.34(7)	0.82(7)	2.17(21)
Hebborn and Capel, 2021 [47]	1.25(12)	1	1.82(18)
Jiang et al., 2025 [25]	1.16(15)	0.68(14)	2.10(42)
Tkachenko et al., 2025 [24]	1.26(7) [a]	1	1.84(1)
Navratil et al., 2026 [26]	1.282	0.96	1.91
^{15}C(5/2$^+$) $^2D_{5/2}$-State, $\sqrt{2k_0} = 0.569$ fm$^{-1/2}$	**ANC, fm$^{-1/2}$**	**S_f**	**C_w**
Mukhamedzhanov et al., 2011 [48]	0.0595(36)	1	0.105(6)
McCleskey et al., 2014 [45]	0.0653(14)	1	0.115(2)
Tkachenko et al., 2025 [24]	0.0740(57) [a]	1	0.130(10)
Navratil et al., 2026 [26]	0.048	0.90	0.089

[a] ANC is recalculated from C_w.

The total cross-section at $E_{\text{c.m.}} = 23.3$ keV serves as a standard benchmark. The corresponding cross-sections $\sigma(23.3\text{ keV})$ are summarized in Table 2.

Table 2. Comparison of ^{14}C$(n,\gamma)^{15}$C cross-sections at $E_{\text{c.m.}} = 23.3$ keV for the capture to the $J^\pi = 1/2^+$ (GS) and $5/2^+$ (1st ES) obtained by different methods.

Reference	σ, μb	Method	^{15}C (J^π)
H. Beer et.al., 1992 [19] [a]	1.72(43)	Direct measurements	$1/2^+$
Herndl et.al., 1999 [49]	6.33	Theory	$1/2^+ + 5/2^+$
Horvath et al., 2002 [20]	2.6(9)	Coulomb dissociation	$1/2^+$
Pramanik, 2002 [50]	4.4(6)	Coulomb dissociation	$1/2^+$
Timofeyuk et al., 2006 [51] [b]	5.3(3)	Theory	$1/2^+$
Reifarth et al., 2008 [22]	5.2(3)	Direct measurements	$1/2^+ + 5/2^+$
Summers and Nunes, 2008 [52]	7.1(5)	Coulomb dissociation	$1/2^+$
Nakamura et al., 2009 [23] [a]	6.1(5)	Coulomb dissociation	$1/2^+$
Esbensen and Reifarth, 2009 [53]	5.2(3)	Coulomb dissociation	$1/2^+$
McCleskey et al., 2014 [45]	5.4(5)	Theory	$1/2^+ + 5/2^+$
Shubhchintak et al., 2014 [34]	7.71	Theory	$1/2^+$
Capel and Nollet, 2017 [54]	4.74(27)	Coulomb dissociation	$1/2^+$
Moschini et al., 2019 [46]	5.8(2)	Theory	$1/2^+ + 5/2^+$
Ma et al., 2020 [27]	4.97(42)	Theory	$1/2^+ + 5/2^+$
Ma et al., 2020 [27]	4.86(48)	*CIAE recommendation*	$1/2^+ + 5/2^+$
Bhattacharyya et al., 2021 [28]	4.4(3)	Theory	$1/2^+$
Jiang et al., 2025 [25]	3.89(76)	Direct measurements	$1/2^+$
Tkachenko et al., 2025 [24]	4.81	Theory	$1/2^+ + 5/2^+$
Navratil et al., 2026 [26]	4.92	Theory	$1/2^+ + 5/2^+$

[a] Maxwellian-averaged cross-section at $kT = 23.3$ keV. [b] Cross-section at a neutron energy of $E_n = 23.3$ keV.

Following Ma et al. [27], we use the China Institute of Atomic Energy (CIAE) recommended value $\sigma(23.3\text{ keV}) = 4.86 \pm 0.48$ μb (10% uncertainty) as a reference range (Figure 1). An extended band of ±20% (4.86 ± 0.96 μb) covers most available experimental and theoretical results.

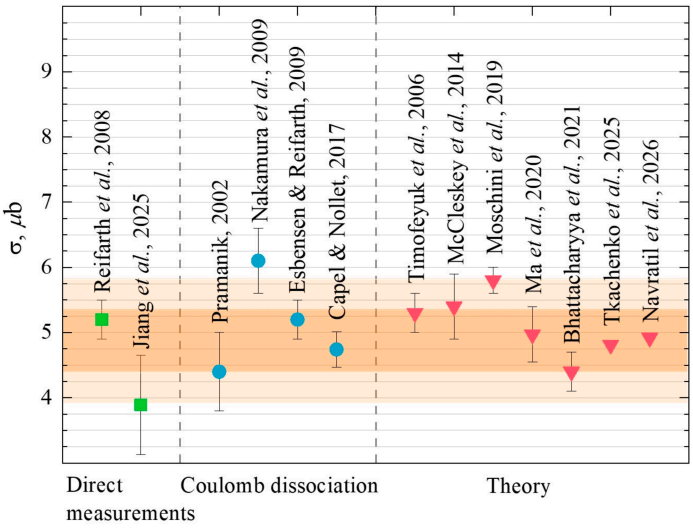


Figure 1. σ(23.3 keV) cross-section of ^{14}C$(n,\gamma)^{15}$C reaction. The inner band refers to the CIAE recommendation 4.86 ± 0.48 μb [27]. An extended band refers to ~20% error, e.g., 4.86 ± 0.96 μb. The data are taken from studies: Reifarth et al., 2008 [22], Jiang et al., 2025 [25] (direct measurements); Pramanik, 2002 [50], Nakamura et al., 2009 [23], Esbensen and Reifarth, 2009 [53], Capel and Nollet, 2017 [54] (Coulomb dissociation); Timofeyuk et al., 2006 [51], McCleskey et al., 2014 [45], Moschini et al., 2019 [46], Ma et al., 2020 [27], Bhattacharyya et al., 2021 [28], Tkachenko et al., 2025 [24], Navratil et al., 2026 [26] (theory).

Figure 2 presents the neutron astrophysical $S_n(E)$-factor $S_n(E) = \sigma(E)/\sqrt{E}$. For the MPCM, Figure 2a shows a ~5% difference between (n,γ_{0+1}) and (n,γ_0) channels across the energy range. Below 10 keV, $S_n(E)$ is nearly constant. Above 10 keV, $S_n(E)$ gradually decreases, with all models showing identical energy dependence up to 1000 keV (Figure 2b). The present MPCM calculations show excellent agreement with Ma et al. [27] (within 5%) and near-exact coincidence with ab initio calculations by Navratil et al. [26].

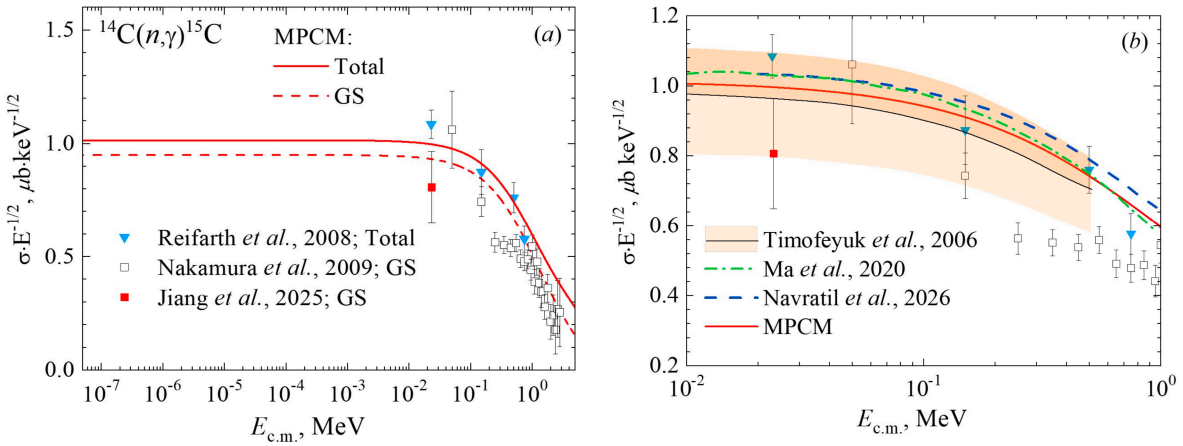


Figure 2. Neutron astrophysical S_n-factor. Experimental data: ▼—Reifarth et al., 2008 [22], □—Nakamura et al., 2009 [23], ■—Jiang et al., 2025 [25]. Theory: (**a**) Comparison of MPCM (n,γ_{0+1}) and (n,γ_0) channels. (**b**) Comparison of MPCM calculations relative to ab initio by Navratil et al. [26], ANC/S_f method by Ma et al. [27], and the charge symmetry method by Timofeyuk et al. [51].

Starting from $E_{c.m.}$ = 10 keV, a gradual decrease of $S_n(E)$ with energy is observed, and as Figure 2b shows, all presented model calculations exhibit the same energy dependence at $E_{c.m.}$ = 10–1000 keV, differing only by small constant factors.

3.2. $n^{14}C$ Capture Reaction Rate

The radiative capture reaction rate for p-wave capture is defined as [3]

$$N_A\langle\sigma v\rangle_{\mathrm{MB}} = 1.1799 \cdot 10^3 \mu^{-1/2} T_9^{-3/2} \int_0^\infty S_n(E) E^{3/2} \exp(-11.605E/T_9) dE \quad (6)$$

where reduced mass μ is in a.m.u., energy E is in MeV, $S_n(E)$ is expressed in μb·keV$^{-1/2}$, the reaction rate $N_A\sigma v_{\mathrm{MB}}$ is in units cm^{3}mol^{-1}s^{-1}, and N_A is the Avogadro number.

The $^{14}C(n,\gamma)^{15}C$ MPCM reaction rate for $T_9 = 0.01$–10 and its comparison with previous works (Appendix B, Table A2) are illustrated in Figure 3. The behavior and comparison of these ratios as a function of temperature is shown in Figure 3. The linear temperature dependence $\sigma v_{\mathrm{MB}} \sim const \cdot T_9$ assumed in Ref. [32] is not supported by full energy-dependent $S_n(E)$ calculations, explaining its deviation at higher T_9.

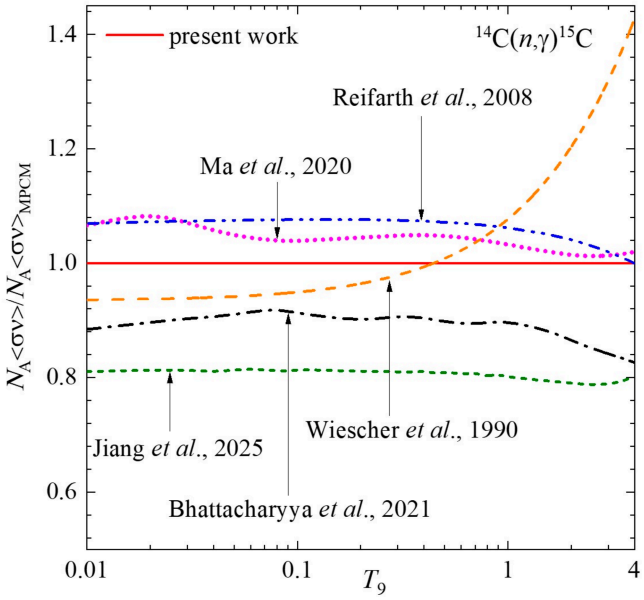


Figure 3. Comparison of the reaction rates from Wiescher et al., 1990 [32] (dashed orange curve), Reifarth et al., 2008 [22] (dashed-double-dotted blue curve), Ma et al., 2020 [27] (dotted magenta curve), Bhattacharyya et al., 2021 [28] (dashed-dotted black curve), and Jiang et al., 2025 [25] (short-dashed green curve) normalized to the MPCM rate.

Since the $S_n(E)$ factors across models are nearly parallel (Figure 2b), the resulting rate ratios remain almost constant over $T_9 = 0.01$–4 (Figure 3). Although ab initio calculations [26,51] do not explicitly report reaction rates, their $S_n(E)$ factors suggest that the corresponding rates would agree with the MPCM results within ~3–4%.

4. $^{14}C(p,\gamma)^{15}N$ Channel

The accumulation of the relatively stable isotope ^{14}C activates the synthesis of elements with A ≥ 12 and contributes to the subsequent production of heavier elements. The neutron radiative capture reaction $^{14}C(n,\gamma)^{15}C$ leads to the formation of the unstable isotope ^{15}C with the half-life $T_{1/2} = 2.449 \pm 0.005$ s (corresponding to a mean lifetime of 3.533 s) and subsequently decays via $^{15}C(\beta^-)^{15}N$. Proton- and alpha-induced radiative capture reactions $^{14}C(p,\gamma)^{15}N$ and $^{14}C(\alpha,\gamma)^{18}O$ produce the stable isotopes ^{15}N and ^{18}O, respectively. Recent investigations of light-mass nuclear reactions have demonstrated their significant impact on r-process abundances [55,56].

The relationship between the charged particle-induced reactions $^{14}C(p,\gamma)^{15}N$ and $^{14}C(\alpha,\gamma)^{18}O$ can be assessed using the corresponding reaction rates evaluated by employing

statistical approaches, specifically Monte Carlo sampling and Bayesian hierarchical models recently reviewed by Iliadis et al. [31], who rigorously quantify reaction rates and their associated uncertainties for stellar modeling.

An overwhelming dominance of the $^{14}C(p,\gamma)^{15}N$ reaction rate over the $^{14}C(\alpha,\gamma)^{18}O$ one is observed throughout the temperature range $T_9 = 0.001$–10 [31]. Therefore, the $^{14}C(p,\gamma)^{15}N$ reaction contributes more efficiently to the destruction of ^{14}C and exhausts the deposit of this isotope more intensively than the (α,γ) process. Since Monte Carlo data for neither the reaction $^{14}C(n,\gamma)^{15}C$, nor ab initio study of $^{14}C(p,\gamma)^{15}N$ analogous to that of Navratil et al. [26], are presently available, it is worthwhile to examine the $^{14}C(p,\gamma)^{15}N$ process using the results obtained within the MPCM approach, presented in Section 3 for the isobar-analogous reaction $^{14}C(n,\gamma)^{15}C$.

4.1. $p^{14}C$ System: Interaction Potentials

Within the MPCM formalism, the interaction potentials for both bound and continuum states are constructed on the basis of the classification of possible orbital states by Young diagrams [39,40,57]. As shown in Ref. [58], the $p^{14}C$ system with orbital angular momenta $L = 0$ and $L = 2$ is described by sufficiently deep potentials containing forbidden states.

The state with orbital momentum $L = 1$ is allowed and corresponds to the $^2P_{1/2}$ ground state of ^{15}N with the quantum numbers J^π, $T = 1/2^-, 1/2$. The parameters of the Gauss potential (3) were fitted to reproduce the binding energy of ^{15}N in the $p + {}^{14}C$ channel $E_b = 10.2074$ MeV [42]. The potential parameters V_0 and α were adjusted so that the asymptotic constant C_w matched the experimental data range of ANC presented in Table 3.

Table 3. Data on ANC and asymptotic constant C_w for the ^{15}N ground state in the $p^{14}C$ channel.

Reference	ANC, fm$^{-1/2}$	S_f	C_w
Timofeyuk et al., 2006 [51]	6.57	0.75–1	1.57(11)
Nassurlla et al., 2023 [59]	6.75(67)	0.75–1	1.62(27)
Ruziev et al., 2024 [60]	7.45(67)	1	1.65(15)

The average ranges for ANC: 6.77–7.37 fm$^{-1/2}$; and C_w: 1.43–1.79.

The final set of V_0 and α potential parameters is presented in Table 4. The calculated charge R_{ch} and matter R_m radii are in good agreement with the experimental values listed in Appendix A. The asymptotic constant $C_w = 1.80(1)$ is also consistent with the range summarized in Table 3.

Table 4. Parameters of the ground state potential for the ^{15}N nucleus in the $p^{14}C$ channel and the corresponding results of MPCM calculations for E_b, R_{ch}, and R_m with the listed parameters V_0 and α.

State	V_0, MeV	α, fm^{-2}	E_b, MeV	R_{ch} (^{15}N), fm	R_m (^{15}N), fm	C_w
$^2P_{1/2}$, GS	221.529718	0.6	10.20740	2.47	2.52	1.80(1)

The set of potential parameters in the continuous spectrum is adjusted to the experimental data on the energy of excited levels E_x (or the resonance energy E_{res} in the center-of-mass) and width $\Gamma_{c.m.}$.

The primary focus is on levels that decay into the proton p-channel and γ-channel with a width of $\Gamma_{c.m.} > 50$–70 keV and with reliably established orbital angular momentum L, total angular momentum J, and parity π. Preference is given to the electric dipole $E1$-transitions corresponding to the $J_i^\pi = 1/2^+$and $3/2^+$ states in the initial scattering channel. Levels with $J_i^\pi = 5/2^\pm$ are excluded from the present consideration as they lead to the $E2$ or $M2$

multipolarity transitions. Finally, there are two resonance states which satisfy declared conditions [41,42]:

1. A $1/2^+$ resonance at $E_x = 11.615(4)$ MeV with a width $\Gamma_{c.m.} = 405(6)$ keV corresponds to $^2S_{1/2}$ state;
2. A $3/2^+$ resonance at $E_x = 13.390(10)$ MeV with a width $\Gamma_{c.m.} = 56(20)$ keV corresponds to $^2D_{3/2}$ state.

Dubovichenko and Dzhazairov-Kakhramanov performed the phase shift analysis of the data on the elastic $^{14}C(p,p)^{14}C$ scattering for the $^2S_{1/2}$ state [61]. The results for the resonance $\delta_{^2S_{1/2}}$ phase shift are presented in Figure 4. The parameters of the interaction potential that reproduce the experimental phase shift are given in Table 5. The parameters of the interaction potential for the $^2D_{3/2}$ scattering state have been fitted to the characteristics of the $3/2^+$ resonance level in the ^{15}N spectrum. The calculated $\delta_{^2D_{3/2}}$ phase shift is presented in Figure 4. Note that both $^2S_{1/2}$ and $^2D_{3/2}$ have a forbidden state; consequently, corresponding phase shifts are normalized following the generalized Levinson theorem [38]. This theorem relates the phase shifts at zero and infinite relative energies through the relation $\delta_L(0) - \delta_L(\infty) = \pi(n+m)$, where n and m are the numbers of allowed and forbidden bound states, respectively, in the partial wave with orbital angular momentum L.

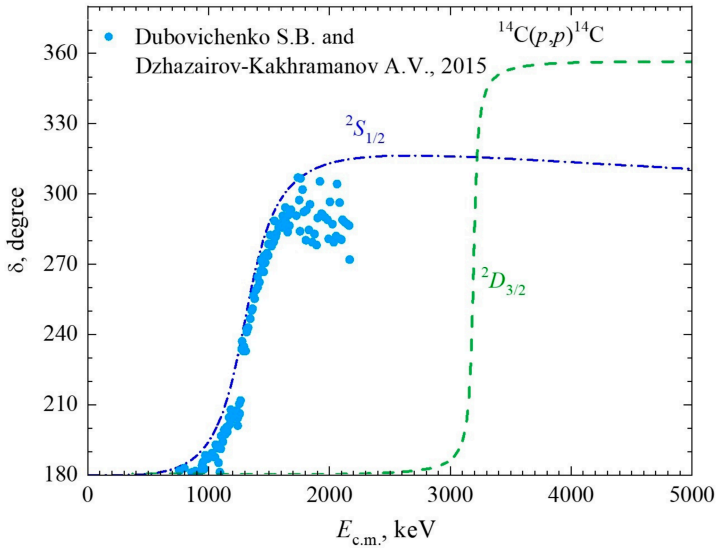


Figure 4. Phase shifts of elastic $^{14}C(p,p)^{14}C$ scattering. The dots show the results of the phase shift analysis from Dubovichenko and Dzhazairov-Kakhramanov, 2016 [61]. Present MPCM calculation of $\delta_{^2S_{1/2}}$ and $\delta_{^2D_{3/2}}$ phase shifts are shown by dashed-dotted and dashed curves, respectively.

Table 5. Characteristics of the continuous spectrum states in the $p^{14}C$ channel. Excitation and resonance energies E_x and E_{res} are in MeV, and the level widths $\Gamma_{c.m.}$ are in keV. Parameters of the interaction potential are V_0 in MeV and α in fm^{-2}. Experimental data are from Ref. [42].

E_x, Exp.	J_i^π, $^{2S+1}L_J$	E_{res}, Exp.	$\Gamma_{c.m.}$, Exp.	V_0	α	E_{res}, Theory	$\Gamma_{c.m.}$, Theory
11.615(4)	$1/2^+$, $^2S_{1/2}$	1.408(4)	405(6)	5037.0	12.0	1.4	535
13.390(10)	$3/2^+$, $^2D_{3/2}$	3.18(1)	56(20)	1421.50	1.1	3.2	53

The potential parameters for the $^2S_{1/2}$ scattering state were slightly revised relative to those used in the earlier work [58]. As a result, the resonance energy is reproduced more accurately, although the calculated resonance width still differs by approximately 30% from the value reported in [41,42]. It should be noted that the obtained value of $\Gamma_{c.m.}(2S_{1/2}) = 535$ keV is directly constrained by reproducing the energy dependence of the experimental

elastic scattering phase shifts $\delta_{2_{S_{1/2}}}$ according to the relationship $\Gamma = 2\left(\frac{d\delta}{dE}\right)^{-1}$ (see Figure 4). A further refinement of the potential parameters would require updated or more detailed phase shift data.

The calculated resonance energy $E_{\rm res}$ and width $\Gamma_{\rm c.m}$ for the $^2D_{3/2}$ state are in good agreement with the experimental data.

4.2. $p^{14}C$ System: Total Cross-Sections and Astrophysical S-Factors

The only data on the total cross-section of the $^{14}C(p,\gamma_0)^{15}N$ reaction available in the EXFOR database [62] are the measurements by Gorres et al. in 1990 [29]. The experimental total cross-section $\sigma(E_{\rm c.m.})$ or the corresponding astrophysical $S(E_{\rm c.m.})$-factor is provided in the energy range of $E_{\rm c.m} = 240$–690 keV [29]. In the framework of the MPCM method, we calculated the total cross-sections for the three partial transitions to the ground state of ^{15}N: $^2S_{1/2} \xrightarrow{E1} {}^2P_{1/2}$, $^2D_{3/2} \xrightarrow{E1} {}^2P_{1/2}$ and $^2P_{3/2} \xrightarrow{M1} {}^2P_{1/2}$. The results are shown in Figure 5. The resonant structure of the $\sigma_{\rm total}$, observed in Figure 5a, is correlated with the energy dependence of the resonant $\delta_{2_{S_{1/2}}}$ and $\delta_{2_{D_{3/2}}}$ phase shifts in Figure 4.

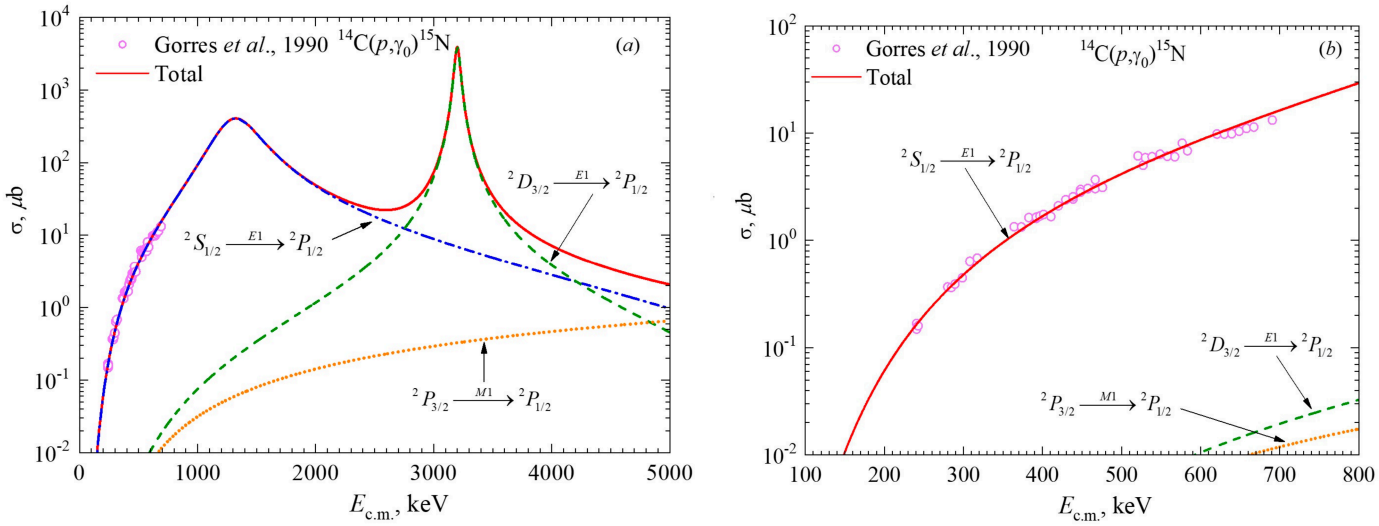


Figure 5. Total and partial cross-sections of the proton radiative capture $^{14}C(p,\gamma_0)^{15}N$. Experimental data are taken from Gorres et al, 1990 [29]. Partial cross-sections are indicated by arrows. MPCM calculations: (**a**) $E_{\rm c.m.} = 140$–5000 keV. (**b**) $E_{\rm c.m.} = 140$–800 keV. Partial and total cross-sections are indicated in the figure field.

To estimate the accuracy of the present calculations, the energy range is narrowed to $E_{\rm c.m.} = 140$–800 keV in Figure 5b. The dominance of the $^2S_{1/2} \xrightarrow{E1} {}^2P_{1/2}$ partial cross-section provides a good agreement with the experimental data [29], so the difference in the $^2S_{1/2}$ resonance widths mentioned above does not affect the cross-section below 800 keV.

To evaluate the impact of this width discrepancy, we performed a sensitivity test by varying the potential parameters V_0 and α to match the narrower width of 405 keV [42]. Although forced parameter fitting lies outside the standard MPCM scheme and degrades the agreement with experimental phase shifts $\delta_{2_{S_{1/2}}}$ (Figure 4), the resulting low-energy cross-section (Figure 5b) below 800 keV shows no significant sensitivity to these variations (deviations do not exceed ~2–3%). Thus, the stellar reaction rates in the region of interest remain quantitatively robust.

The MPCM methodology provides a reliable framework and is sufficiently well developed to reproduce the experimental data for the $^{14}C(p,\gamma_0)^{15}N$ reaction cross-section at higher energies, should such measurements become available in the future.

The astrophysical S-factors were calculated from the corresponding cross-sections according to the standard definition [3,31]:

$$S(E) = Ee^{2\pi\eta}\sigma(E). \quad (7)$$

Here, the Sommerfeld parameter η is expressed numerically in Ref. [31] as

$$2\pi\eta = 0.989510 Z_1 Z_2 \sqrt{\frac{\mu}{E}} \quad (8)$$

Figure 6 presents the astrophysical S-factors calculated from the cross-sections shown in Figure 5.

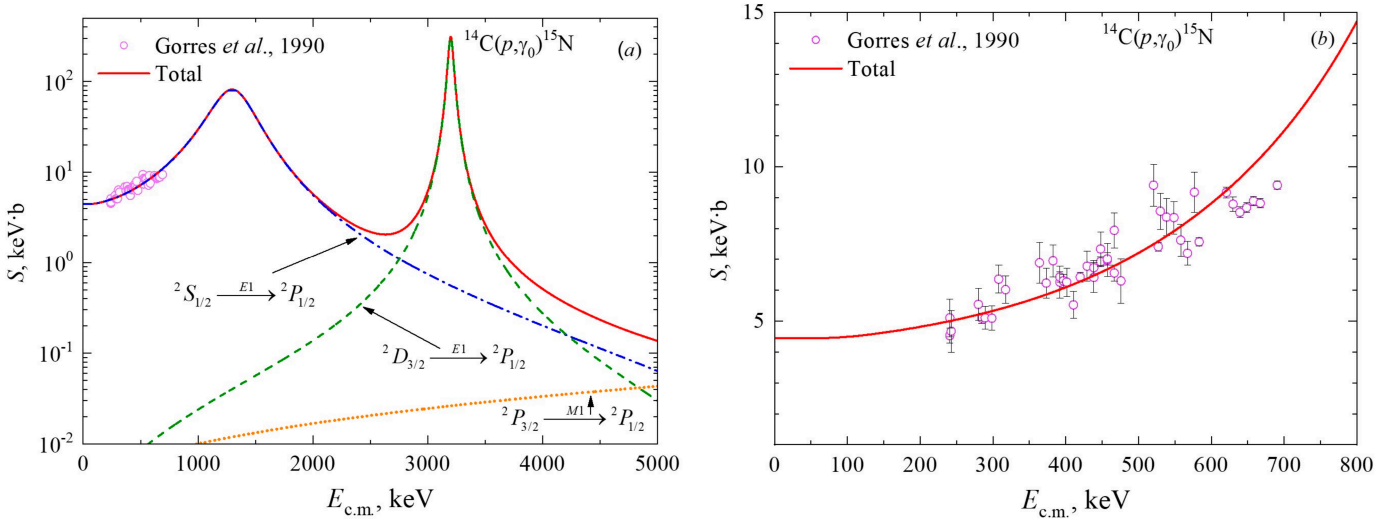


Figure 6. Astrophysical S-factor of the proton radiative capture $^{14}C(p,\gamma_0)^{15}N$. Experimental data are from Gorres et al., 1990 [29]. Partial S-factors are indicated by arrows. MPCM calculations: (**a**) $E_{c.m.}$ = 140–5000 keV. (**b**) $E_{c.m.}$ = 140–800 keV.

In the energy range below $E_{c.m.}$ ~ 100–140 keV, the value of the calculated S-factor remains almost constant and equal to 4.5(1) keV·b, see Figure 6b. Thus, the astrophysical S-factor at zero energy for the radiative capture reaction $^{14}C(p,\gamma_0)^{15}N$ can be estimated as $S(0) \simeq 4.5(1)$ keV·b.

In Figure 7, our astrophysical S-factor results are compared with those reported in previous studies. A parameterization of the energy dependence of the S-factor below $E_{c.m.}$ = 1 MeV suggested by Gorres et al. [29] leads to $S(0) \simeq 7.5$ keV·b. An initial study of $^{14}C(p,\gamma_0)^{15}N$ reaction by the Monte Carlo method was performed 20 years later by Iliadis et al. [30], who presented the parameterized S-factor along with the reaction rate. From the analytical expression of Ref. [30], it follows that $S(0) \simeq 5.24$ keV·b. The band in Figure 7 corresponds to the digitized data from Ref. [63]; the authors position their results as a fit to experimental data [29], and they suggest a value of the S-factor at the lowest energy, $E_{c.m.} \simeq 100$ keV, to be $S(0) \simeq 5.66^{+0.87}_{-0.81}$ keV · b.

The presented data on the $S(0)$-factor are fairly consistent, except for those of Gorres et al. [29]. Our method suggests a lower value of $S(0) = 4.5(1)$ keV·b, which differs by ~15% different from the value by Iliadis et al. [30]. The energy dependence of the S-factors, shown in Figure 7b as the ratio S/S_{MPCM} at the $E_{c.m.} \leq 1000$ keV, appears somewhat questionable. It is possible that this behavior reflects interpolation errors in the corresponding calculations, whereas our results are obtained without the use of any interpolation procedure.

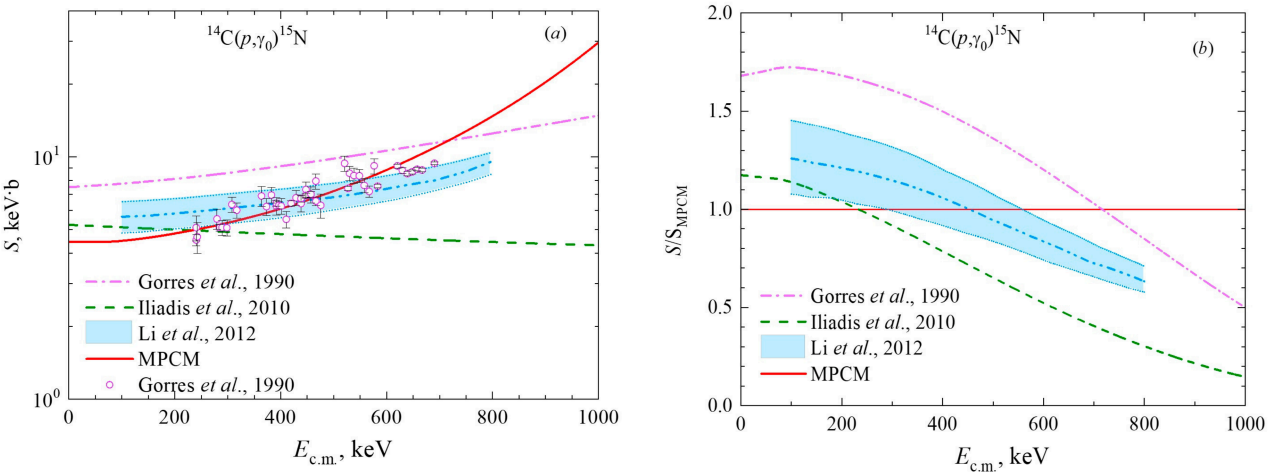


Figure 7. (**a**) Comparison of the MPCM astrophysical *S*-factor of the proton radiative capture $^{14}C(p,\gamma_0)^{15}N$ with the previous works: Gorres et al. [29]—dashed-dotted curve; Iliadis et al. [30]—dashed curve; Li et al. [63]—blue band. (**b**) Ratio of *S*-factors from panel (**a**) to the MPCM data.

The experimental database for the $^{14}C(p,\gamma_0)^{15}N$ reaction remains limited. The available cross-section measurements used in the present analysis were reported by Gorres et al. [29] in 1990 and cover the center-of-mass energy interval $E_{c.m.}$ = 240–690 keV. Although the MPCM calculations reproduce the general energy dependence and magnitude of these measurements, the absence of direct experimental information below 240 keV represents an important limitation for the quantitative validation of the calculated astrophysical *S*-factor in the low-energy region.

New experimental measurements extending below the presently available energy interval would be particularly valuable for constraining the low-energy behavior of the astrophysical *S*-factor and testing the predicted contributions of individual electromagnetic transitions. Measurements with improved statistical and systematic precision would also facilitate a more reliable assessment of the uncertainties associated with the calculated stellar reaction rates.

4.3. p^{14}C System: Reaction Rates

The reaction rate of the proton radiative capture on the carbon isotope ^{14}C with the formation of ^{15}N in the ground state is calculated using the total cross-section shown in Figure 5a in the range of temperatures T_9 = 0.01–10. In Figure 8, our MPCM reaction rate is presented along with the recent reaction rate evaluation for the $^{14}C(p,\gamma_0)^{15}N$ by Iliadis et al. (2026) [31]. An earlier publication by Iliadis et al. (2010) [30] and the latest one represents the development of the application of the Monte Carlo method to the processing of experimental data on reactions with charged particles of astrophysical interest. Following [31], the method can be illustrated using the example of the $^{14}C(p,\gamma_0)^{15}N$ reaction. The astrophysical *S*-factors measured in the energy range $E_{c.m}$ = 240–690 keV [29] are interpolated, while extrapolation is applied at energies below and above this interval. The evaluated cross-sections are used to numerically estimate thermonuclear reaction rates, which are represented by three levels: low, medium, and high. Such a representation provides the shaded band in Figures 8 and 9.

The inset in Figure 8 illustrates the range of low temperatures T_9 = 0.01–0.03, relevant to hydrogen burning in the solar and stellar CNO cycles. An extreme decrease in the rate from ~10^{-10} to ~10^{-18} cm^{3}mol^{-1}s^{-1} is observed. This result may serve as an argument for assessing the relative differences in rates obtained using different methods. It is obvious

that a difference in rates within one or two orders of magnitude is more than acceptable. In general, the Monte Carlo reaction rate is slightly higher than the MPCM rate up to $T_9 = 2.5$. For more details, we present the ratio of rates from Refs. [29–31] to that of the present work in Figure 9. Note that this information is provided in Table A4, Appendix C.

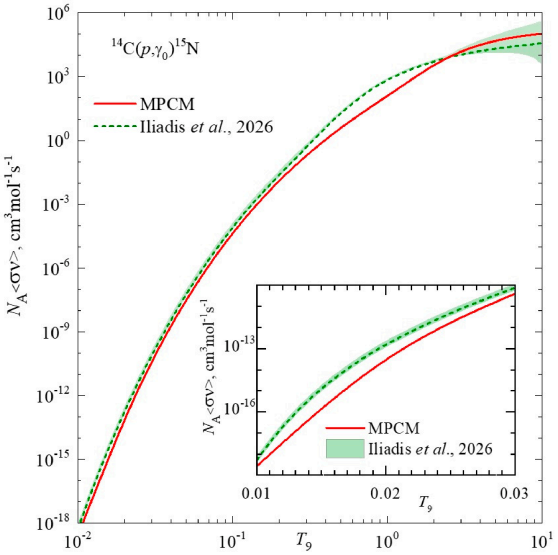


Figure 8. Reaction rate of the radiative proton capture ^{14}C(p,γ_0)^{15}N. Theory: red solid curve—present MPCM calculations with the total cross-section in Figure 5a; the green band refers to Monte Carlo reaction rate by Iliadis et al. [31]. The inset shows the temperature range $T_9 = 0.01$–0.03.

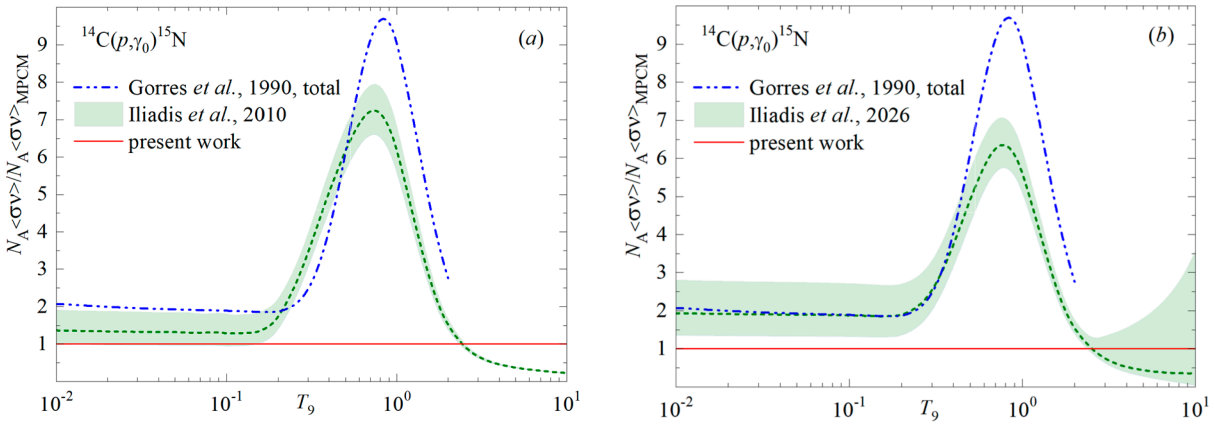


Figure 9. Comparison of ^{14}C(p,γ_0)^{15}N reaction rates via the ratio to the MPCM rate in Figure 8. Gores et al. [29]—dashed double-dotted curve; (**a**) the band corresponds to the reaction rate ratio reported by Iliadis et al. (2010) [30]; (**b**) the band corresponds to the reaction rate ratio reported by Iliadis et al. (2026) [31].

Let us denote the Monte Carlo cross-section, S-factors, and reaction rate as MC for short. The discussion of the ratios in Figure 9 concerns the temperatures close to $T_9 \sim 1$, where a visual difference in rates is revealed. To clarify this situation, we turn to the comparison of MPCM and MC methods. We found the following distinctions between MPCM and MC, which may turn essential in consequences:

1. The calculation procedure designated in Refs. [30,31] is based on the subdivision of the constituent cross-sections (and corresponding reaction rates) into the sum of direct capture (DC) and resonant ones: $\sigma_{MC}(E) = \sigma_{DC} + \sigma_R$. Such a presentation assumes the interference between σ_{DC} and σ_R, but as declared in [31], interference effects have been ignored.

In the framework of MPCM, there is no such subdivision in principle. We examine this issue in detail on the example of the $^{15}N(p,\gamma)^{16}O$ reaction in [64]. In short, the omission of interference effects may lead to significant changes in computing quantities, such as phase shifts, transition amplitudes, etc.

2. The MC calculations of direct capture cross-sections σ_{DC} are performed with zero interaction potentials in the scattering channel, and radial wave functions are taken simply as regular Coulomb functions $F_l(kr)$.

In contrast, MPCM $^2S_{1/2}$ and $^2D_{3/2}$ scattering functions $\chi_i(r)$ in $p + ^{14}C$ channel corresponding to the $^2S_{1/2}$ and $^2D_{3/2}$ waves have an *internal node* as they are generated with deep attractive potentials with a forbidden state and do not coincide with $F_l(kr)$ functions. Therefore, we believe that σ_{DC} is overestimated at low energies and underestimated at higher energies.

3. In Ref. [31], along with the calculated reaction rate of $^{14}C(p,\gamma_0)^{15}N$ process, the fractions of DC and resonant constituents into the total rate are presented in Figure 16. Let us discuss separately the contribution of each resonance incorporated into the MC calculations, since we identify the primary cause of the difference in reaction rates depicted in Figure 9.

We refer to the five resonances included in MC calculations as $J^\pi(E_{c.m.},\text{keV})$. Resonances $5/2^-(243)$ and $3/2^+(597)$ make a minor contribution to the rate because of their small widths $\Gamma_{c.m.} < 0.5$ keV and <1 eV, respectively. Following MC estimations, the major resonances are: $5/2^+(326)$ with unknown width; $3/2(495)$ with assigned parity $\pi = -1$ and width $\Gamma_{c.m.} = 0.2$ keV; regarding $1/2^+(1408)$ with $\Gamma_{c.m.} = 405(6)$ keV, we also consider this resonance. Note that the $3/2^+(3180)$ resonance, which we considered, is not accounted for in the MC calculated reaction rate.

In summary, the concern is the $3/2(495)$ resonance, which mainly causes the difference in the rate ratio illustrated in Figure 9. The key question revolves around establishing the parity of this level. Iliadis et al. [31] followed Ajzenberg-Selove data [42], where the 495 keV resonance is assigned as a negative parity state $3/2^-$. Thus, it is a $P_{3/2}$-wave, which corresponds to the magnetic dipole transition $^2P_{3/2} \overset{M1}{\rightarrow}{}^2P_{1/2}$, but, as seen in Figure 6b, there is no explicit evidence of such a resonance at $E_{c.m.} \sim 500$ keV. The 495 keV resonance turned out to be a real puzzle when Szücs and Mohr published their research findings [65]. They confidently identified this level as a positive parity state $3/2^+$ corresponding to the dominant D-component. It means that a strong dipole $E1$-transition $^2D_{3/2} \overset{E1}{\rightarrow}{}^2P_{1/2}$ should provide the partial cross-section at these energies. However, Szücs and Mohr [65] invalidated any essential input into the reaction rate for both $M1$- and $E1$-transitions, as the reliably determined width of the 495 keV level $\Gamma_p = 493.6 \pm 75.3$ meV (1 keV = 10^6 meV) is approximately 400 times smaller than the commonly accepted value of $\Gamma_p = 0.2$ keV.

Adopting the proton width $\Gamma_p = 493.6 \pm 75.3$ meV from Szücs and Mohr [65] reduces the resonance contribution by a factor of ~400 compared with the standard evaluation ($\Gamma_p = 0.2$ keV) [31,42]. Such a small width renders the 495 keV resonance contribution to the total cross-section and reaction rate practically negligible. In the present MPCM framework, where the $P_{3/2}$ potential is constrained by zero elastic scattering phase shifts, no pronounced resonance peak is generated at $E_{c.m.}$~500 keV (Figure 6b), which naturally agrees with the suppressed resonance input implied by the Szücs and Mohr findings.

5. Comparison of $^{14}C(n,\gamma)^{15}C$ and $^{14}C(p,\gamma)^{15}N$ Reaction Rates

Nuclear reaction rates are conventionally calculated by averaging the reaction cross-section over the Maxwell–Boltzmann energy distribution of interacting particles in a thermalized plasma. In contrast, Tsallis statistics introduces a non-extensive parameter q, leading to

deviations from the Maxwellian distribution. Consequently, reaction rates obtained within the Tsallis framework may differ from the standard Maxwell–Boltzmann rates, particularly for reactions sensitive to the high-energy tail of the particle distribution.

In the present section, we compare the ^{14}C$(n,\gamma)^{15}$C and ^{14}C$(p,\gamma)^{15}$N reaction rates calculated with the MPCM method. The discussion is organized in terms of the non-extensivity parameter q. The case of conventional Maxwell–Boltzmann statistics corresponds to the value $q = 1$ and serves as the reference for analyzing non-extensive effects observed in Tsallis statistics at $q \neq 1$.

5.1. Reaction Rates in the Maxwell–Boltzmann Framework

The commonly used formal analysis of proton radiative capture reaction rates is performed in terms of the Gamow peak energy $E_0 = \left[\left(\frac{\pi}{\hbar}\right)^2 (Z_1 Z_2 e^2)^2 \frac{\mu}{2} (k_B T)^2\right]^{\frac{1}{3}}$ and the Gamow window $E_0 \pm$ D/2, where $\Delta = \frac{4}{\sqrt{3}}\sqrt{E_0 k_B T}$ [3]. The Gamow window defines the energy range centered at E_0 that gives the maximum contribution to the reaction rate of the total cross-sections at a given temperature T_9.

By analogy, for the neutron-induced (n,γ) processes, the effective energy $E_{\rm eff}$ and the window defined as *full width at half maximum* (FWHM) are compared with the Gamow peak E_0 and Gamow window $\Delta E_{\rm FWHM}$. Along with the FWHM, the root mean square value or the standard deviation $\Delta E_{\rm rms}$ of the energy distribution centered at $E_{\rm eff}$ is used. We suggest the following set of approximations:

$$E_{\rm eff} = (l + 1/2)k_B,\ \Delta E_{\rm FWHM} \simeq 2\sqrt{(l+1/2)\ln 2}k_B T\ ,\ \text{and}\ \Delta E_{\rm rms} = \sqrt{l+1/2}k_B T. \quad (9)$$

These analytical relations are validated if the cross-section has a power law energy dependence $\sigma(E)\sim E^{l-1/2}$ for the partial orbital angular momentum l in the initial scattering channel $n + A$.

Figure 10 illustrates the range of effective energies $E_{\rm eff}$ and E_0 for the ^{14}C$(n,\gamma)^{15}$C and ^{14}C$(p,\gamma)^{15}$N reactions, respectively. These windows rather accurately define the range of neutron and proton $E_{\rm c.m.}$ energies, which contribute most significantly to a value of temperature T_9 in stellar media. That also serves as a guide to the measured or computed cross-sections required for obtaining accurate reaction rate values. Our consideration of ^{14}C$(n,\gamma)^{15}$C reaction in Section 3 concludes that cross-sections of this reaction are substantiated theoretically quite well in the energy range $E_{\rm c.m.} \lesssim 1000$ keV, which is sufficient, as can be seen from Figure 10b. Note that $E_{\rm eff}$, directly determined as the position of the maximum of the integrands, fits the calculated approximate value $E_{\rm eff} = 3/2k_B T$ near exactly up to $T_9 = 1$–2. The shift of $E_{\rm eff}$ to lower energies is observed at higher temperatures, while it is determined directly from the integrands, and reaches 18–20% on the energy scale at $T_9 = 4$.

The situation with the ^{14}C$(p,\gamma)^{15}$N reaction is somewhat different. In Section 4, we show that the astrophysical S-factor is nearly constant up to 100–140 keV. This matches the windows in the temperature range $T_9 = 0.01$–0.15, as shown in Figure 10c. Since the Coulomb barrier in the $p + {}^{14}$C channel is $B_{Coul} \simeq 2$ MeV, the cross-section at low energies is so small that the reaction rate drops by orders of magnitude at these values of T_9. The cross-section measured by Görres et al. [29], at $E_{\rm c.m.} = 240$–700 keV, covers the windows corresponding to $T_9 \simeq 1$–2.8 as shown in Figure 10d. For the purposes of the present study, this level of accuracy is sufficient.

Figure 11 presents a comparison of the ^{14}C$(n,\gamma)^{15}$C and ^{14}C$(p,\gamma)^{15}$N radiative capture reaction rates calculated within the Maxwell–Boltzmann framework over the temperature range $T_9 = 0.01$–10. The green shaded vertical area corresponds to the temperatures $T_9 \sim 0.02$–0.15 typical of hydrogen burning in AGB stars and the neutron-induced cycle,

both of which lead to the production of the ^{15}N isotope. At the edge points of $T_9 = 0.02$ and 0.15, the ratio of reaction rates $R_{(n,\gamma)/(p,\gamma)} = \sigma v_{^{14}C(n,\gamma)^{15}C} / \sigma v_{^{14}C(p,\gamma)^{15}N}$ is pointed.

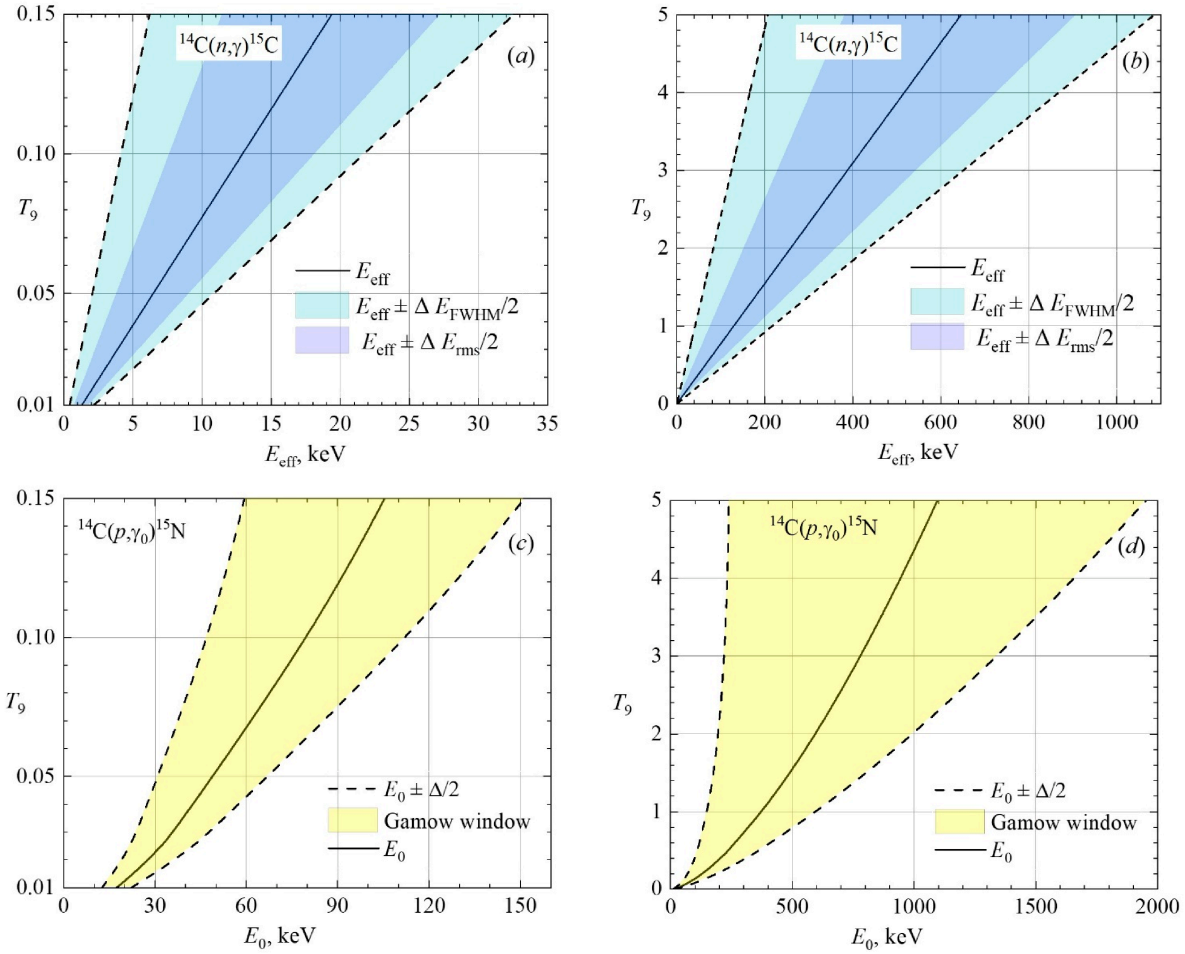


Figure 10. Gamow-like windows of $^{14}C(n,\gamma)^{15}C$ and Gamow windows $^{14}C(p,\gamma)^{15}N$ reactions. The corresponding notations are provided within the figure panels. (**a**) $^{14}C(n,\gamma)^{15}C$ Gamow-like window for E_{eff} = 0–15 keV; (**b**) $^{14}C(n,\gamma)^{15}C$ Gamow-like window for E_{eff} = 0–1000 keV; (**c**) $^{14}C(p,\gamma)^{15}N$ Gamow window for E_0 = 0–150 keV; (**d**) $^{14}C(p,\gamma)^{15}N$ Gamow window for E_0 = 0–2000 keV.

The dominance of radiative neutron captures over the hydrogen burning rate results in orders of magnitude $R_{(n,\gamma)/(p,\gamma)} \simeq 10^{14}$–$10^5$. Such a ratio suggests another perspective on the scenario of ^{15}N formation, conditioned by the neutron-to-proton concentrations ratio n_n/n_p in the stellar environment. Production of nitrogen isotope ^{15}N occurs via the $^{14}C(n,\gamma)^{15}C(\beta^-)^{15}N$ reaction, predominantly even in the case of $n_n < n_p$ within orders of magnitude, since this is compensated by large values of the reaction rate ratio $R_{(n,\gamma)/(p,\gamma)}$.

The cross-point T_9, corresponding to the equality of $\sigma v_{^{14}C(n,\gamma)^{15}C} = \sigma v_{^{14}C(p,\gamma)^{15}N}$ reaction rates, is referred to hereafter as $T_9^{c.p.}$. The efforts to determine and discuss the location of $T_9^{c.p.}$ were initiated by Wiescher et al. [32]. Based on the parameterization of $^{14}C(n,\gamma)^{15}C$ and $^{14}C(p,\gamma)^{15}N$ reaction rates from [32], Kawano et al. [33] determined $T_9^{c.p.} = 1.5$. The recent study by Shubhchintak et al. [34] is based on the analysis of the neutron capture $^{14}C(n,\gamma)^{15}C$ rates taken from the following Refs.: Beer et al. [19], Descouvemont [66], Horvath et al. [20], and Reifarth et al. [22]. The rate of (n,γ) reaction in Ref. [34] is calculated using the capture cross-section extracted from the Coulomb breakup spectra and is also included in the comparison with the $^{14}C(p,\gamma)^{15}N$ rate calculated by Kawano et al. [33]. The range reported by Shubhchintak et al. [34] is $T_9^{c.p.} = 0.9$–1.7 (see Table 6 for details).

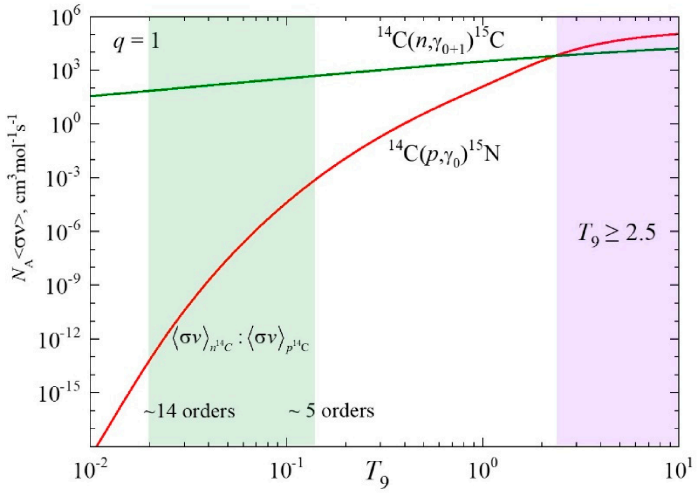


Figure 11. MPCM calculations of the reaction rates of the $^{14}C(n,\gamma_{0+1})^{15}C$ (green solid curve) and $^{14}C(p,\gamma_0)^{15}N$ (red solid curve) processes. The green shaded leftward vertical area corresponds to the AGB temperatures T_9 ~ 0.02–0.15, typical for the thermonuclear reactions. The shaded region on the right side indicates the T_9 where (p,γ_0) rate exceeds (n,γ_{0+1}) rate.

Table 6. Data on the temperature cross-point $T_9^{c.p.}$.

Maxwell–Boltzmann Statistics	$T_9^{c.p.}$	Tsallis Statistics, Present Work	$T_9^{c.p.}$
Wiescher et al., 1990 [32]	1.5	$q = 0.95$	1.7
Beer et al., 1992 [19]	0.9	$q = 0.9$	1.4
Descouvemont, 2000 [66]	1.7	$q = 1.05$	2.8
Horvath et al., 2002 [20]	1.1	$q = 1.1$	3.2
Reifarth et al., 2008 [22]	1.5		
Shubhchintak et al., 2014 [34]	1.4		
Present work	2.5		

To summarize the presented early results, it is important to note that they are based on different model data for reaction rates that do not align with one another. We propose an essentially different approach to conducting such an analysis. In Figure 11, the shaded region on the right side indicates the interval of temperatures $T_9 \geq 2.5$, where the (p,γ_0) rate exceeds the (n,γ_{0+1}) rate, both calculated in the same MPCM approach. Therefore, a value of $T_9^{c.p.} = 2.5$ is observed, which is higher than the values reported in the above studies. We consider this result to be more reliable and internally consistent, since both the $^{14}C(n,\gamma)^{15}C$ and $^{14}C(p,\gamma)^{15}N$ reaction rates are obtained within the framework of the same theoretical model.

5.2. Phenomenological Sensitivity of Reaction Rates to Tsallis Statistics

In a recent paper [24], we studied the consequence of non-extensive Tsallis statistics on the rate of $^{14}C(n,\gamma)^{15}C$ reaction [24]. The application of Tsallis statistics in the present study is intended as a phenomenological investigation of the sensitivity of astrophysical reaction rates to possible deviations from the Maxwell–Boltzmann energy distribution. The non-extensivity parameter q is treated as an adjustable parameter characterizing the assumed statistical distribution rather than as a directly measurable quantity or a parameter derived from the microscopic properties of stellar plasma. In particular, the values $q = 0.90$, 0.95, 1.05, and 1.10 are selected to illustrate the response of the calculated reaction rates to moderate variations around the Maxwell–Boltzmann limit $q = 1$. These values should not be interpreted as predictions of the actual statistical state of any specific astrophysical environment. It is therefore natural to apply the same computational approach to the

proton capture reaction $^{14}C(p,\gamma)^{15}N$. We follow the formalism by Hou et al. [67,68] while modifying the reaction rate with the following energy distribution:

$$f_q(E) = B_q 4\left(\frac{\mu}{2\pi k_B T}\right)^{\frac{1}{2}} \frac{E}{k_B T}\left[1-(q-1)\frac{E}{k_B T}\right]^{\frac{1}{q-1}} \quad (10)$$

Here, q is a non-extensive parameter; explicit expressions for the normalizing constant B_q may be found in Ref. [24]. Transition to the extensive Maxwell–Boltzmann energy distribution $f_{\mathrm{MB}}(E)$ is provided while $+q = 1$, so that $\lim_{q\to 1}\frac{1}{q-1}\ln\left[1-(q-1)\frac{E}{k_B T}\right] = -\frac{E}{k_B T}$.

The modified expression for the reaction rate is of the form:

$$N_A\langle\sigma v\rangle_q = N_A\left(\frac{8}{\pi\mu}\right)^{1/2}(k_B T)^{-3/2} B_q \int_0^{E_{\max}} \sigma(E) E\left[1-(q-1)\cdot\frac{E}{k_B T}\right]^{\frac{1}{q-1}} dE \quad (11)$$

The upper limit in integral depends on the non-extensive parameter: if $+q < 1$, then $E_{\max} = \infty$; if $q > 1$, then $E_{\max} = \frac{1}{q-1}k_B T$, $k_B T = 0.086173 \cdot T_9$ (MeV).

We propose to illustrate the q-effect using the neutron window transformation. The evaluation of the effective energy and Gamow-like windows leads to the following relations:

$$E_{\mathrm{eff},q} = \frac{(l+1/2)k_B T}{1+(l+1/2)(q-1)},\ \Delta E_{\mathrm{rms},q} = k_B T\sqrt{\frac{l+1/2}{[1+(l+1/2)(q-1)]^3}},$$
$$\text{and } \Delta E_{\mathrm{FWHM},q} \approx 2\sqrt{\ln 2}\,\Delta E_{\mathrm{rms},q} \quad (12)$$

Figure 12 is analogous to Figure 10a,b, calculated for the orbital angular momentum $l = 1$. The effective energy $E_{\mathrm{eff},q}$ and window width $\Delta E_{\mathrm{rms},q}$ presented in Figure 12 refer to the q values in pairs $q = 1 \pm 0.05$ and $q = 1 \pm 0.10$, corresponding to 5% and 10% deviation from the extensive Maxwell–Boltzmann case. We do not present the curves for the $E_{\mathrm{eff},q} \pm \Delta E_{\mathrm{FWHM},q}/2$ windows to avoid overloading the figure. One may notice a rather moderate transformation of the windows in Figure 12, comparing Figure 10a,b. This finding supports the conclusion from our previous research presented in [24], which states that the non-extensity effect in the $^{14}C(n,\gamma)^{15}C$ reaction appears as an increase of the Maxwell–Boltzmann reaction rate by a factor of approximately 1.35 or a decrease by a factor of about 0.8 when $0.9 < q < 1.1$.

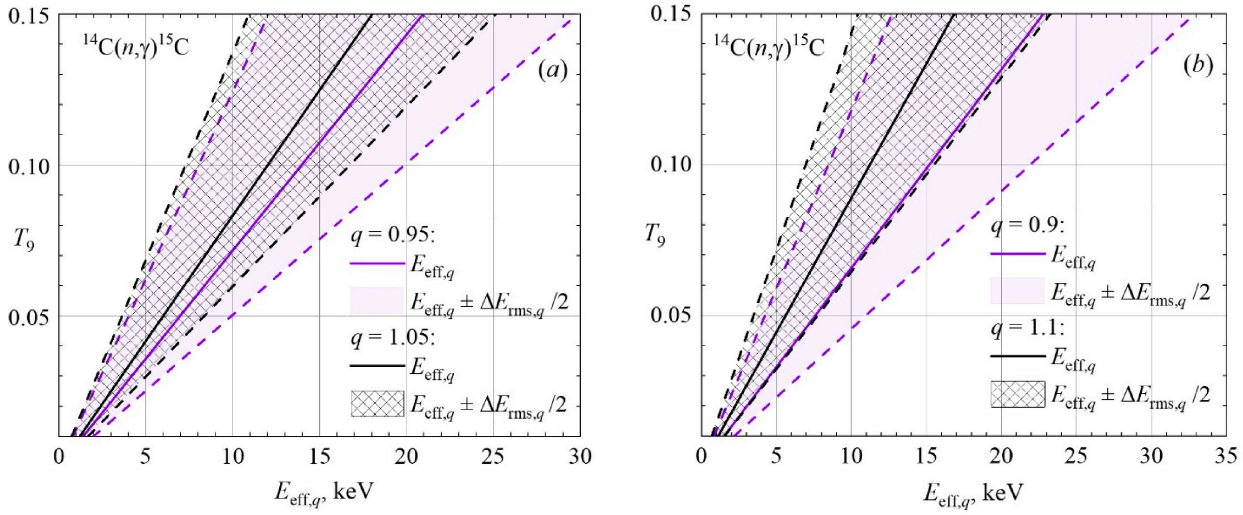


Figure 12. Gamow-like windows of $^{14}C(n,\gamma)^{15}C$ reaction corresponding to the Tsallis non-extensive q-distribution. The corresponding notations are provided within the figure panels. (**a**) $q = 0.95$ and 1.05; (**b**) $q = 0.9$ and 1.1.

The situation with the $^{14}C(p,\gamma)^{15}N$ reaction is more complicated. The process of obtaining an analog of the Gamow peak energy E_0 and the associated window width Δ relies on expanding the integrand function in Expression (11) into a Taylor series. The problem is the choice of a small expansion parameter. Therefore, to avoid the approximation uncertainties, we present in Figure 13 the integrands $I_q(E)$ of Relation (11) calculated with the cross-section $\sigma(E)$ from Section 4. The maximum of $I_q(E)$ corresponds to the exact Gamow peak energy $E_{0,q}$.

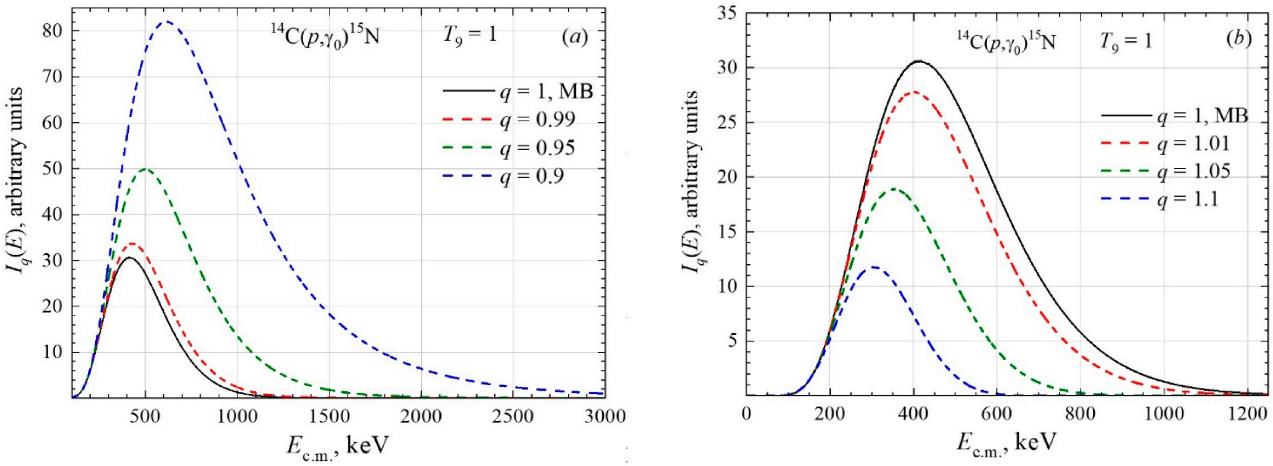


Figure 13. Integrands $I_q(E)$ of the $^{14}C(p,\gamma)^{15}N$ reaction rate. Comparison of Maxwell–Boltzmann and Tsallis statistics for $T_9 = 1$: (**a**) $q = 1$ (MB) and $q < 1$; (**b**) $q = 1$ (MB) and $q > 1$.

Setting $T_9 = 1$ highlights the shift of the Gamow peak $E_{0,q}$ position, depending on the q parameter value compared with the Maxwell–Boltzmann E_0. In Figure 13a, it can be seen that when the parameter q decreases by 1%, 5%, and 10%, the Gamow peak $E_{0,q}$ shifts to the region of higher energies and the Gamow window Δ_q expands. The results shown in Figure 13b correspond to symmetrically increased values of the non-extensivity parameter q. In this case, the opposite trend is observed: the effective energy $E_{0,q}$ shifts toward lower energies, while the width of the Gamow window, Δ_q, becomes narrower. We present in Figure 13 the results for a 1% deviation from the Maxwell–Boltzmann case to illustrate the visual non-extensive effect observed even with a very small violation of extensity in the case of charged particles interaction in the initial $p + {}^{14}C$ channel. The integral outcome reveals itself in the reaction rates shown in Figure 14.

Variation of parameter q simulates a violation of the equilibrium state of stellar plasma. A rise in $^{14}C(p,\gamma)^{15}N$ reaction rates by an order of magnitude is observed in Figure 14a,c for $q = 0.95$ and 0.9, and vice versa, a decrease of rates is seen in Figure 14b,d for $q = 1.05$ and 1.9 at low temperatures $T_9 \lesssim 0.2$.

The comparison of $^{14}C(n,\gamma)^{15}C$ and $^{14}C(p,\gamma)^{15}N$ reaction rates can be quantified through the ratio $R_{(n,\gamma)/(p,\gamma)}$ evaluated at the boundary temperatures $T_9 = 0.02$ and 0.15. The degree of the $^{14}C(n,\gamma)^{15}C$ predominance may be estimated based on the following summary of the results presented in Figures 11 and 14:

$$q = 1\text{: } R_{(n,\gamma)/(p,\gamma)} \simeq 10^{14}\text{–}10^{5}\ \text{(MB)};$$

$$q = 0.95\text{: } R_{(n,\gamma)/(p,\gamma)} \simeq 10^{11}\text{–}10^{4};\ q = 1.05\text{: } R_{(n,\gamma)/(p,\gamma)} \simeq 10^{18}\text{–}10^{6};$$

$$q = 0.9\text{: } R_{(n,\gamma)/(p,\gamma)} \simeq 10^{8}\text{–}10^{3};\ q = 1.1\text{: } R_{(n,\gamma)/(p,\gamma)} \simeq 10^{21}\text{–}10^{7}.$$

We see the substantial variety in the relative contribution of $^{14}C(n,\gamma)^{15}C$ and $^{14}C(p,\gamma)^{15}N$ processes in the production of ^{15}N nuclei, depending on the state of stellar plasma under the given conditions defined via the q parameter.

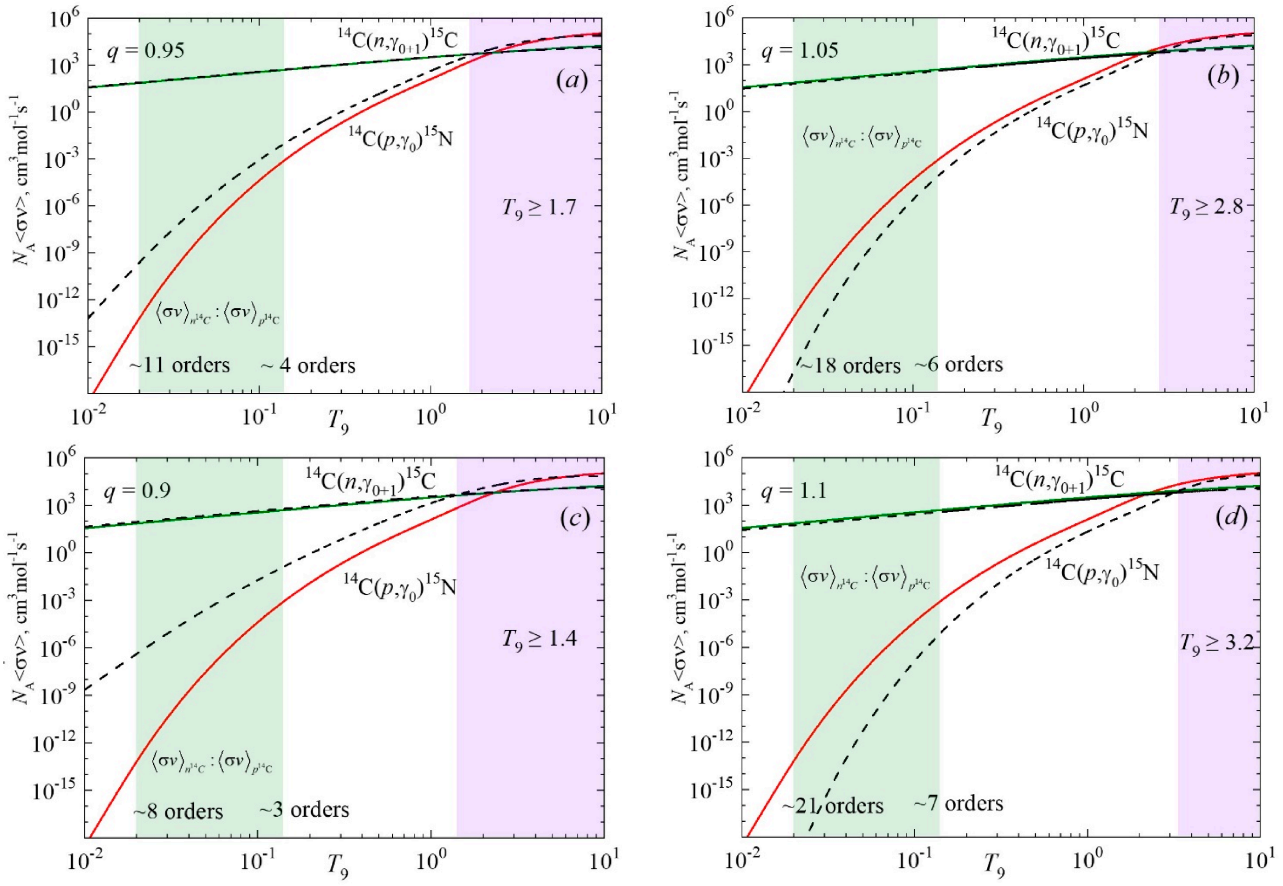


Figure 14. Comparison of $^{14}C(n,\gamma)^{15}C$ (green solid curve) and $^{14}C(p,\gamma)^{15}N$ (red solid curve) reaction rates: Maxwell–Boltzmann statistics—solid curves; Tsallis statistics—dashed curves. Shaded areas are as in Figure 11. (**a**) $q = 0.95$; (**b**) $q = 1.05$; (**c**) $q = 0.9$; (**d**) $q = 1.1$.

In Section 5.1, we discuss the origin of the data on the crossing point $T_9^{c.p.}$, corresponding to the equality of the rates $\sigma v_{(n,\gamma)} = \sigma v_{(p,\gamma)}$ and reported earlier. Table 6 lists all available data on $T_9^{c.p.}$. The MPCM results are presented for both statistics. In the case of $q < 1$, the $^{14}C(p,\gamma)^{15}N$ reaction becomes dominant at temperatures $T_9 > 1.7$ or $T_9 > 1.4$, which is lower than that obtained within Maxwell–Boltzmann statistics, which shows $T_9 > 2.5$. As for the $q > 1$, this energy range shifts to the higher $T_9 > 2.8$ or $T_9 > 3.2$.

It should be noted that the non-extensivity parameter q does not represent a directly measurable physical quantity and cannot presently be derived from first principles. Rather, it serves as a phenomenological parameter that enables the modeling of deviations from the Maxwell–Boltzmann distribution. Within this framework, values of $q < 1$ generally lead to an enhancement of the reaction rate, whereas values of $q > 1$ result in its suppression.

Finally, tabulated numerical values of the $^{14}C(n,\gamma)^{15}C$ and $^{14}C(p,\gamma)^{15}N$ reaction rates calculated within the framework of the non-extensive Tsallis statistics are provided in Appendix D.

6. Physical Constraints, State Dependence, and Predictive Character of the MPCM

An important feature of the MPCM is that the parameters of the interaction potentials for the individual partial waves are determined a priori from independent physical information rather than adjusted to reproduce radiative capture observables. For bound states, the potentials are constrained by the experimental binding energies, charge or matter radii, and asymptotic normalization coefficients, whereas continuum-state potentials are constrained

by elastic scattering phase shifts and, where applicable, by the measured energies and widths of resonant states. Consequently, the potential parameters are not fitted to the calculated radiative capture cross-sections, astrophysical S-factors, or reaction rates.

The state dependence of the interaction potentials is an intrinsic feature of the MPCM and should not be interpreted as an arbitrary parametrization. Different partial waves are characterized by different orbital symmetries, spin and total angular momentum, numbers of Pauli-forbidden states, binding energies, and scattering properties. These differences impose distinct physical constraints on the corresponding effective interactions. In addition, the neutron- and proton-induced channels differ because of the Coulomb interaction and the properties of their respective bound states. It is therefore physically expected within the MPCM that different quantum states and reaction channels are described by different effective potentials.

Once these potentials have been determined from the independent bound- and scattering state observables, the corresponding radial wave functions are obtained and used to evaluate the electromagnetic transition matrix elements. The radiative capture cross-sections, astrophysical S-factors, and thermonuclear reaction rates then follow without any further adjustment of the interaction potential parameters to the capture observables. In this sense, the calculated capture quantities constitute predictions of the model subject to the independently imposed spectroscopic and scattering constraints.

A particular advantage of the present approach is that the competing ^{14}C$(n,\gamma)^{15}$C and ^{14}C$(p,\gamma)^{15}$N reactions are treated consistently within the same theoretical framework. Previous estimates of their competition relied on reaction rates obtained using different theoretical approaches. Such comparisons may inherit systematic differences associated with the underlying reaction models. By calculating both reactions within the MPCM, the present treatment reduces this source of model-dependent systematic uncertainty and permits a more internally consistent determination of the temperature at which the two reaction rates become equal.

The principal result of the present work is therefore the first self-consistent determination, within a common theoretical framework, of the transition temperature between the competing ^{14}C$(n,\gamma)^{15}$C and ^{14}C$(p,\gamma)^{15}$N reactions. We obtain $T_9^{\mathrm{c.p.}}$, which is higher than the previously reported estimates. The difference reflects, at least in part, the use of reaction rates calculated consistently within the same MPCM framework rather than rates assembled from different theoretical descriptions.

An important limitation of the present investigation is the restricted experimental information available for both radiative capture reactions. In particular, the ^{14}C$(p,\gamma)^{15}$N calculations are primarily constrained by the measurements of Görres et al. [29] over the center-of-mass energy interval 240–690 keV, while the experimental information for the ^{14}C$(n,\gamma)^{15}$C reaction provides only limited constraints on the full energy dependence of the capture cross-section. Consequently, theoretical extrapolations into experimentally unexplored energy regions remain subject to model-dependent uncertainties. New high-precision measurements at lower center-of-mass energies are therefore strongly needed to constrain the astrophysical S-factor for proton capture, validate the low-energy neutron capture cross-section, and improve the reliability of the corresponding stellar reaction rates. Such experimental advances would provide an important foundation for more accurate modeling of nucleosynthesis processes involving ^{14}C.

7. Concluding Remarks

Finally, tabulated numerical values of the ^{14}C$(n,\gamma)^{15}$C and ^{14}C$(p,\gamma)^{15}$N reaction rates calculated within the framework of the non-extensive Tsallis statistics are provided in Appendix D. In the present work, we perform a comparative study of ^{14}C$(n,\gamma)^{15}$C$(\beta^-)^{15}$N

and $^{14}C(p,\gamma_0)^{15}N$ reactions, which contribute to the nucleosynthesis of the isotope ^{15}N, using a consistent framework. The total cross-sections of these reactions have been calculated within the same MPCM approach. This allows for a consistent evaluation of the corresponding reaction rates computed and compared in both Maxwell–Boltzmann and Tsallis non-extensive statistics.

Our recent comprehensive study of $^{14}C(n,\gamma_{0+1})^{15}C$ reaction [24] has now been complemented by the recently published works of Jiang et al. [25], Navratil et al. [26], and Kim et al. [55]. Our results demonstrate excellent agreement with deviations of ~3–5% in the neutron astrophysical S_n-factor, compared with the recent ab initio theoretical studies on this reaction [26]. That is a reason for a slight reconsideration of the claim in Ref. [25] that their results for the $^{14}C(n,\gamma_{0+1})^{15}C$ reaction rate are definitive and highly precise, since our calculated rate exceeds their recommended values by approximately 20%. This difference is also directly relevant to the nucleosynthesis study of Kim et al. [55]. Using the reaction rate from [25], the sensitivity of the main r-process to the $^{14}C(n,\gamma)^{15}C$ reaction was estimated at 16% enhancement of the yields of nuclei in the mass region $25 < A < 75$. The present 20% refinement of the $^{14}C(n,\gamma)^{15}C$ reaction rate may lead to reevaluation of the astrophysical consequences.

We quantify the comparison of the $^{14}C(n,\gamma)^{15}C$ and $^{14}C(p,\gamma)^{15}N$ reactions by the ratio of their rates $R_{(n,\gamma)/(p,\gamma)}$. The evaluated value at the boundary temperatures $T_9 = 0.02$ and 0.15 relevant for the ^{15}N formation of ^{15}N in AGB stars results in orders of magnitude $R_{(n,\gamma)/(p,\gamma)} \simeq 10^{14}$–$10^5$ in the case of the equilibrium state of stellar plasma. This ratio suggests an alternative perspective on the scenario of ^{15}N formation, conditioned by the concentration of neutrons n_n relative to protons n_p in the stellar environment. The production of nitrogen isotope ^{15}N may proceed predominantly through $^{14}C(n,\gamma)^{15}C(\beta^-)^{15}N$ reaction, even when $n_n < n_p$ by several orders of magnitude, since the lower neutron concentration can be compensated by the significantly larger ratio $R_{(n,\gamma)/(p,\gamma)}$ of the neutron and proton capture reaction rates.

The floating value of the temperature crossing point $T_9^{\text{c.p.}}$ within the range $T_9^{\text{c.p.}} = 0.9$–1.7 reported by Shubhchintak et al. [34] is conditioned by the comparison of the single-out $\sigma v_{(p,\gamma)}$ reaction rate by Wiescher et al. [32] with a set of *different neutron-induced rates* $\sigma v_{(n,\gamma)}$. In our case, we are operating with a nearly precisely determined rate within ~3–5% accuracy of the $^{14}C(n,\gamma_{0+1})^{15}C$ rate $\sigma v_{(n,\gamma)}$. Therefore, the floating of the over-cross point determined in the MPCM approach as $T_9^{\text{c.p.}} = 2.5$ may appear through the refinement of the proton radiative capture rate. We see the following eventual and desirable corrections for the $^{14}C(p,\gamma)^{15}N$ reaction: extension of the range of the measured cross-sections; independent additional investigation of the $3/2(E_{\text{c.m}} = 495$ keV) resonance assignments; and phase shift analysis for the proposed interaction by an MPCM resonating $\delta_{2_{D_{3/2}}}$ phase shift.

All the above remarks are based on the rates of reactions $^{14}C(n,\gamma)^{15}C$ and $^{14}C(p,\gamma)^{15}N$, calculated within the conventional Maxwell–Boltzmann framework corresponding to non-extensivity parameter value $q = 1$. We simulated the conditions for thermonuclear reactions in a weakly non-equilibrium plasma by varying the parameter q by 5–10% from unity. As shown in Ref. [24], the moderate dependence of the $^{14}C(n,\gamma)^{15}C$ reaction rate was found. Regarding the $^{14}C(p,\gamma)^{15}N$ process, the reaction rate changes by several orders of magnitude when q ranges from 0.9 to 1.1.

In the case of $0.9 < q < 0.95$, the $^{14}C(p,\gamma)^{15}N$ reaction rate becomes dominant over the $^{14}C(n,\gamma)^{15}C$ rate at temperatures $1.4 < T_9 < 1.7$, which is lower than what Maxwell–Boltzmann statistics shows, which is $T_9 > 2.5$. As for $1.05 < q < 1.1$, a shift to higher temperatures, $2.8 < T_9 < 3.2$, is revealed. Therefore, the non-extensive state of stellar plasma may lead to either the additional production of ^{15}N in the $^{14}C(p,\gamma)^{15}N$ reaction, or its input may turn out to be negligible. That is especially important in the temperature range

$T_9 \approx 0.02$–0.15, relevant to the competition between neutron and proton radiative capture on ^{14}C, which provides the synthesis of ^{15}N in stellar CNO and HCNO cycles.

The results obtained within the Tsallis framework demonstrate the sensitivity of the competing neutron and proton capture reaction rate coefficients to the assumed statistical energy distribution. Since the non-extensivity parameter is not independently constrained for the astrophysical environments considered, these findings should be interpreted as conditional phenomenological results rather than definitive predictions of non-equilibrium stellar reaction rates.

Author Contributions: Methodology, N.A.B. and S.B.D.; Software, S.B.D.; Validation, R.Y.K. and B.M.Y.; Formal Analysis, N.A.B. and B.B.B.; Investigation, R.Y.K. and B.M.Y.; Resources, R.Y.K. and B.M.Y.; Data Curation, B.B.B.; Writing—Original Draft, S.B.D.; Writing—Review and Editing, A.S.T. and N.A.B.; Visualization, A.S.T.; Supervision, N.A.B.; Project Administration, S.B.D. All authors have read and agreed to the published version of the manuscript.

Funding: This research was funded by the Science Committee of the Ministry of Science and Higher Education of the Republic of Kazakhstan, Grant No. AP23486219.

Data Availability Statement: The original contributions presented in the study are included in the article. Further inquiries can be directed to the corresponding authors.

Conflicts of Interest: The authors declare no conflicts of interest. The funders had no role in the design of the study; in the collection, analyses, or interpretation of data; in the writing of the manuscript; or in the decision to publish the results.

Appendix A. Input Data for the $N + {}^{14}$C Channel

Table A1. Input information for the $N + {}^{14}$C channel.

	Values	References
Masses m, a.m.u.		
Proton	1.007276466621(53)u	Navas et al., 2024 [69]
Neutron	1.0086649160(5)u	Navas et al., 2024 [69]
^{14}C	14.003242u	Chart of nucleus shape and size parameters ($0 \leq Z \leq 14$) [70,71]
Magnetic moments μ, μ_N is nuclear magneton		
Proton	$2.7928473446(8)\mu_N$	Navas et al., 2024 [69]
Neutron	$-1.9130427(5)\mu_N$	Navas et al., 2024 [69]
^{14}C	0	
Matter radii R_m, fm		
Proton	0.8409(4)	Navas et al., 2024 [69]
Neutron	0.8409(4)	Navas et al., 2024 [69]
^{14}C	2.619(57)	Liatard et al., 1990 [72]
	2.47	Wang et al., 2001 [73]
	2.619(57)	Ozawa et al., 2001 [74]
	2.30(7)	Ozawa et al., 2001 [75]
	2.33(7)	Kanungo et al., 2016 [76]
	2.44(6)	Ahmad et al., 2017 [77]
	2.42(5)	Dobrovolsky et al., 2021 [78]
	2.34	Rahi and Flaiyh, 2022 [79]
	2.259(18)	Mouadil et al., 2024 [80]
	2.367(35)	Li et al., 2025 [81]

Table A1. *Cont.*

	Values	References
^{15}C	2.783(92)	Liatard et al., 1990 [72]
	2.40(5)	Ozawa et al., 1996 [82]
	2.59	Wang et al., 2001 [73]
	2.783(92)	Ozawa et al., 2001 [74]
	2.50(8)	Ozawa et al., 2001 [75]
	2.54(4)	Kanungo et al., 2016 [76]
	2.59(3)	Ahmad et al., 2017 [77]
	2.59(5)	Dobrovolsky et al., 2021 [78]
	2.78	Rahi and Flaiyh, 2022 [79]
	2.450(33)	Mouadil et al., 2024 [80]
	2.509(40)	Li et al., 2025 [81]
^{15}N	2.52	Wang et al., 2001 [73]
	2.42(10)	Ozawa et al., 2001 [75]
	2.56(10)	Ahmad et al., 2017 [77]
	2.42	Abdullah and Abdullah, 2022 [83]
Charge radii R_{ch}, fm		
Proton	0.8409(4)	Navas et al., 2024 [69]
^{14}C	2.48(9)	Yamaguchi et al., 2011 [84]
	2.50(13)	Zhao et al., 2023 [85]
	2.45(20)	Zhao et al., 2024 [86]
^{15}C	2.47(8)	Yamaguchi et al., 2011 [84]
	2.56(27)	Zhao et al., 2023 [85]
	2.56(20)	Zhao et al., 2024 [86]
^{15}N	2.42(10)	Ozawa et al., 2001 [75]
	2.47(8)	Yamaguchi et al., 2011 [84]
	2.59(9)	Zhao et al., 2023 [85]
	2.58(16)	Zhao et al., 2024 [86]
Binding energy E_b, MeV		
n^{14}C	1.2181 (GS)	Ajzenberg-Selove, 1991 [42]
	0.5781 (1st ES)	Ajzenberg-Selove, 1991 [42]
p^{14}C	10.2074	Ajzenberg-Selove, 1991 [42]
Constant	$\hbar^2/m_0 = 41.4686$ MeV·fm^2, $m_0 = 931.494$ MeV/c^2 is a.m.u.	

Appendix B. ^{14}C(n,γ)^{15}C Radiative Capture Reaction Rates

Table A2. ^{14}C(n,γ)^{15}C radiative capture MPCM reaction rate with comparison to the previous results obtained for the Maxwell–Boltzmann statistics. $N_A\langle\sigma v\rangle$ is provided in cm^{3}mol^{-1}s^{-1}.

T_9	$N_A\langle\sigma v\rangle$	Ratio				
		Wiescher et al., 1990 [32]	Reifarth et al., 2008 [22]	Ma et al., 2020 [27]	Bhattacharyya et al., 2021 [28]	Jiang et al., 2025 [25]
0.01	3.57×10^1	0.94	1.07	1.07	0.88	0.81
0.02	7.12×10^1	0.94	1.07	1.09	0.90	0.81
0.03	1.07×10^2	0.94	1.07	1.07	0.90	0.81
0.04	1.42×10^2	0.94	1.07	1.06	0.91	0.81
0.05	1.77×10^2	0.94	1.07	1.05	0.91	0.81
0.06	2.12×10^2	0.94	1.08	1.04	0.91	0.81
0.07	2.47×10^2	0.94	1.08	1.04	0.92	0.81
0.08	2.82×10^2	0.95	1.08	1.04	0.92	0.81
0.09	3.17×10^2	0.95	1.08	1.04	0.92	0.81

Table A2. *Cont.*

T_9	$N_A\langle\sigma v\rangle$	Ratio				
		Wiescher et al., 1990 [32]	Reifarth et al., 2008 [22]	Ma et al., 2020 [27]	Bhattacharyya et al., 2021 [28]	Jiang et al., 2025 [25]
0.1	3.52×10^2	0.95	1.08	1.04	0.91	0.81
0.15	5.23×10^2	0.96	–	–	–	0.81
0.2	6.92×10^2	0.96	1.08	1.04	0.90	0.81
0.25	8.59×10^2	0.97	–	–	–	0.81
0.3	1.02×10^3	0.98	1.08	1.05	0.91	0.81
0.35	1.18×10^3	0.99	–	–	–	0.81
0.4	1.34×10^3	0.99	1.07	1.05	0.90	0.81
0.45	1.50×10^3	1.00	–	–	–	0.81
0.5	1.66×10^3	1.01	1.07	1.05	0.90	0.81
0.55	1.81×10^3	1.02	–	–	–	0.81
0.6	1.96×10^3	1.02	1.07	1.05	0.89	0.81
0.65	2.11×10^3	1.03	–	–	–	0.81
0.7	2.25×10^3	1.04	1.07	1.04	0.89	0.81
0.75	2.40×10^3	1.04	–	–	–	0.80
0.8	2.54×10^3	1.05	1.07	1.04	0.90	0.80
0.85	2.68×10^3	1.06	–	–	–	0.80
0.9	2.82×10^3	1.06	1.06	1.04	0.90	0.80
0.95	2.96×10^3	1.07	–	–	–	0.80
1	3.10×10^3	1.08	1.06	1.03	0.90	0.80
2	5.55×10^3	1.20	1.04	1.01	0.86	0.79
2.5	6.61×10^3	1.26	1.03	1.01	0.85	0.79
3	7.59×10^3	1.32	1.02	1.01	0.84	0.79
3.5	8.50×10^3	1.37	1.01	1.02	0.83	0.79
4	9.35×10^3	1.43	1.00	1.02	0.83	0.80
5	1.09×10^4	1.53	–	1.03	0.81	–
6	1.23×10^4	1.63	–	–	–	–
7	1.36×10^4	1.72	–	–	–	–
8	1.47×10^4	1.82	–	–	–	–
9	1.57×10^4	1.92	–	–	–	–
10	1.65×10^4	2.02	–	–	–	–

We performed an approximation of the GS $^{14}C(n,\gamma)^{15}C$ reaction rate and the total rate (provided in Table A2):

$$N_A\langle\sigma v\rangle = a_1/T_9^{2/3}\exp(-a_2/T_9^{1/3})(1.0+a_3T_9^{1/3}+a_4T_9^{2/3}+a_5T_9+a_6T_9^{4/3}+a_7T_9^{5/3})+a_8T_9^{a_9}. \quad \text{(A1)}$$

The total and GS reaction rate approximation parameters a_i at 5% accuracy are given in Table A3.

Table A3. Analytical parameterization equation (A1) parameters of the $^{14}C(n,\gamma)^{15}C$ reaction rate.

i	a_i (Total)	a_i (GS)
1	964.222	945.5511
2	4.94155	5.09723
3	0.29088	−3.27812
4	−16.5326	−0.26229
5	−20.09722	−32.1241
6	−7.71086	−11.40699
7	−8.33403	−7.33743
8	3411.508	3168.048
9	0.99366	0.98569
	$\chi^2 = 0.0008$	$\chi^2 = 0.0005$

Calculation of χ^2 is implemented following the standard definition:

$$\chi^2 = \frac{1}{N}\sum_{i=1}^{N}\left[\frac{\langle\sigma v\rangle_i^{app.}(T_9) - \langle\sigma v\rangle_i^{calc.}(T_9)}{\Delta\langle\sigma v\rangle_i^{calc.}(T_9)}\right]^2 = \frac{1}{N}\sum_{i=1}^{N}\chi_i^2, \quad \text{(A2)}$$

where N is the number of the calculation points; $\langle\sigma v\rangle_i^{app.}(T_9)$ is the approximated reaction rate; $\langle\sigma v\rangle_i^{calc.}(T_9)$ is calculated reaction rate; the error $\Delta\langle\sigma v\rangle_i^{calc.}(T_9)$ we assume here to be 5% of the calculated reaction rate.

Appendix C. $^{14}C(p,\gamma)^{15}N$ Radiative Capture Reaction Rates

Table A4. $^{14}C(p,\gamma)^{15}N$ radiative capture MPCM reaction rate with comparison to the previous results obtained for the Maxwell–Boltzmann statistics. $N_A<\sigma v>$ is provided in $cm^3mol^{-1}s^{-1}$.

T_9	$N_A<\sigma v>$	Ratio				
		Wiescher et al., 1990 [32] and Gorres et al., 1990 [29]			Iliadis et al., 2010 [30]	Iliadis et al., 2026 [31]
		Non-Resonant [32]	Resonant [29]	Total		
0.01	2.65×10^{-19}	2.07	6.26×10^{-141}	2.07	1.36	1.93
0.02	8.76×10^{-14}	1.99	3.80×10^{-64}	1.99	1.34	1.91
0.03	4.05×10^{-11}	1.96	1.72×10^{-39}	1.96	1.33	1.90
0.04	1.92×10^{-9}	1.94	1.47×10^{-27}	1.94	1.32	1.90
0.05	2.95×10^{-8}	1.93	1.28×10^{-20}	1.93	1.32	1.89
0.06	2.37×10^{-7}	1.92	4.01×10^{-16}	1.92	1.31	1.89
0.07	1.24×10^{-6}	1.91	5.28×10^{-13}	1.91	1.30	1.89
0.08	4.87×10^{-6}	1.90	9.96×10^{-11}	1.90	1.31	1.88
0.09	1.54×10^{-5}	1.90	5.24×10^{-9}	1.90	1.32	1.88
0.1	4.16×10^{-5}	1.89	1.15×10^{-7}	1.89	1.28	1.88
0.11	9.89×10^{-5}	1.88	1.34×10^{-6}	1.88	1.28	1.87
0.12	2.13×10^{-4}	1.88	9.78×10^{-6}	1.88	1.29	1.87
0.13	4.22×10^{-4}	1.87	5.04×10^{-5}	1.87	1.29	1.86
0.14	7.81×10^{-4}	1.87	1.98×10^{-4}	1.87	1.31	1.86
0.15	1.37×10^{-3}	1.85	6.25×10^{-4}	1.85	1.31	1.85
0.16	2.28×10^{-3}	1.86	1.67×10^{-3}	1.86	1.36	1.85
0.18	5.64×10^{-3}	1.84	8.06×10^{-3}	1.85	1.48	1.86
0.2	1.23×10^{-2}	1.83	2.66×10^{-2}	1.86	1.69	1.88
0.25	5.84×10^{-2}	1.81	1.92×10^{-1}	2.00	2.48	2.07
0.3	1.92×10^{-1}	1.78	6.23×10^{-1}	2.40	3.43	2.50
0.35	4.96×10^{-1}	1.75	1.34	3.09	4.31	3.08
0.4	1.09×10^{0}	1.72	2.29	4.01	5.08	3.72
0.45	2.12×10^{0}	1.69	3.37	5.06	5.66	4.35
0.5	3.78×10^{0}	1.66	4.47	6.13	6.20	4.93
0.6	9.87×10^{0}	1.59	6.42	8.01	6.93	5.82
0.7	2.15×10^{1}	1.51	7.73	9.24	7.29	6.31
0.8	4.17×10^{1}	1.43	8.33	9.76	7.22	6.40
0.9	7.41×10^{1}	1.34	8.32	9.66	6.82	6.14
1	1.24×10^{2}	1.24	7.90	9.14	6.24	5.65
1.25	3.70×10^{2}	0.99	6.05	7.04	4.40	4.13
1.5	9.06×10^{2}	0.79	4.28	5.06	2.97	2.85
1.75	1.88×10^{3}	0.64	3.03	3.67	2.04	2.01
2	3.41×10^{3}	0.54	2.22	2.76	1.47	1.50
2.5	8.22×10^{3}	–	–	–	0.90	0.99
3	1.50×10^{4}	–	–	–	0.65	0.73
3.5	2.29×10^{4}	–	–	–	0.53	0.60
4	3.13×10^{4}	–	–	–	0.45	0.52
5	4.79×10^{4}	–	–	–	0.37	0.43
6	6.30×10^{4}	–	–	–	0.32	0.39
7	7.64×10^{4}	–	–	–	0.28	0.37

Table A4. *Cont.*

T_9	$N_A<\sigma v>$	Ratio				
		Wiescher et al., 1990 [32] and Gorres et al., 1990 [29]			Iliadis et al., 2010 [30]	Iliadis et al., 2026 [31]
		Non-Resonant [32]	Resonant [29]	Total		
8	8.80×10^4	–	–	–	0.26	0.36
9	9.79×10^4	–	–	–	0.24	0.36
10	1.06×10^5	–	–	–	0.22	0.36

The numerical MPCM $^{14}C(p,\gamma_0)^{15}N$ Maxwell–Boltzmann averaged reaction rate provided in Table A4 is parametrized by the form:

$$N_A\langle\sigma v\rangle = \frac{a_1}{T^{b_1}}\exp\left(-\frac{a_2}{T^{b_2}}\right)\left(1 + a_3T^{b_3} + a_4T^{b_4} + a_5T^{b_5} + a_6T^{b_6} + a_7T^{b_7}\right) + \frac{a_8}{T^{b_8}}\exp\left(-\frac{a_9}{T^{b_9}}\right) \quad \text{(A3)}$$

with parameters a_i and b_i being listed in Table A5.

Table A5. Analytical parameterization equation. (A3) parameters of the $^{14}C(p,\gamma_0)^{15}N$ reaction rate.

i	a_i	b_i
1	−13.87945	1.105309
2	13.57990	0.3273575
3	5.613876×10^{-9}	−6.351922
4	-1.162993×10^7	1.051155
5	-2.411727×10^6	1.358957
6	9.628110×10^6	1.333300
7	-1.453575×10^6	1.354842
8	4.644946×10^7	1.863525
9	14.89739	0.7833696
	$\chi^2 = 0.09$	

Appendix D. Non-Extensive Tsallis Statistics

Table A6. $^{14}C(n,\gamma_{0+1})^{15}C$ and $^{14}C(p,\gamma_0)^{15}N$ reaction rates $N_A<\sigma v>$ calculated for non-extensive Tsallis statistics (q = 0.95–1.1).

T_9	$N_A<\sigma v>$, cm^{3}mol^{-1}s^{-1}							
	q = 0.95		q = 0.9		q = 1.05		q = 1.1	
	$n^{14}C$	$p^{14}C$	$n^{14}C$	$p^{14}C$	$n^{14}C$	$p^{14}C$	$n^{14}C$	$p^{14}C$
0.01	3.81×10^1	6.02×10^{-14}	4.45×10^1	2.20×10^{-9}	2.97×10^1	1.40×10^{-24}	2.67×10^1	2.00×10^{-29}
0.02	7.61×10^1	2.72×10^{-10}	8.87×10^1	4.31×10^{-7}	5.93×10^1	3.34×10^{-17}	5.34×10^1	2.16×10^{-20}
0.03	1.14×10^2	2.12×10^{-8}	1.33×10^2	8.00×10^{-6}	8.88×10^1	8.95×10^{-14}	8.00×10^1	2.85×10^{-16}
0.04	1.52×10^2	3.65×10^{-7}	1.76×10^2	5.83×10^{-5}	1.18×10^2	1.15×10^{-11}	1.06×10^2	9.19×10^{-14}
0.05	1.89×10^2	2.88×10^{-6}	2.20×10^2	2.57×10^{-4}	1.48×10^2	3.43×10^{-10}	1.33×10^2	5.03×10^{-12}
0.06	2.26×10^2	1.43×10^{-5}	2.63×10^2	8.35×10^{-4}	1.77×10^2	4.41×10^{-9}	1.59×10^2	1.01×10^{-10}
0.07	2.64×10^2	5.22×10^{-5}	3.06×10^2	2.20×10^{-3}	2.06×10^2	3.32×10^{-8}	1.86×10^2	1.06×10^{-9}
0.08	3.01×10^2	1.53×10^{-4}	3.49×10^2	4.99×10^{-3}	2.35×10^2	1.73×10^{-7}	2.12×10^2	7.19×10^{-9}
0.09	3.38×10^2	3.84×10^{-4}	3.92×10^2	1.01×10^{-2}	2.64×10^2	6.89×10^{-7}	2.38×10^2	3.56×10^{-8}
0.1	3.74×10^2	8.53×10^{-4}	4.34×10^2	1.88×10^{-2}	2.93×10^2	2.25×10^{-6}	2.64×10^2	1.40×10^{-7}
0.11	4.11×10^2	1.72×10^{-3}	4.76×10^2	3.27×10^{-2}	3.22×10^2	6.29×10^{-6}	2.90×10^2	4.55×10^{-7}
0.12	4.47×10^2	3.21×10^{-3}	5.18×10^2	5.37×10^{-2}	3.50×10^2	1.56×10^{-5}	3.16×10^2	1.29×10^{-6}
0.13	4.83×10^2	5.62×10^{-3}	5.60×10^2	8.42×10^{-2}	3.79×10^2	3.49×10^{-5}	3.42×10^2	3.24×10^{-6}

Table A6. *Cont.*

T_9	$N_A\langle\sigma v\rangle$, cm^{3}mol^{-1}s^{-1}							
	$q = 0.95$		$q = 0.9$		$q = 1.05$		$q = 1.1$	
	n^{14}C	p^{14}C	n^{14}C	p^{14}C	n^{14}C	p^{14}C	n^{14}C	p^{14}C
0.14	5.20×10^{2}	9.34×10^{-3}	6.02×10^{2}	1.27×10^{-1}	4.08×10^{2}	7.19×10^{-5}	3.68×10^{2}	7.39×10^{-6}
0.15	5.56×10^{2}	1.49×10^{-2}	6.43×10^{2}	1.85×10^{-1}	4.36×10^{2}	1.38×10^{-4}	3.94×10^{2}	1.56×10^{-5}
0.16	5.91×10^{2}	2.27×10^{-2}	6.84×10^{2}	2.63×10^{-1}	4.64×10^{2}	2.52×10^{-4}	4.19×10^{2}	3.07×10^{-5}
0.18	6.63×10^{2}	4.84×10^{-2}	7.66×10^{2}	4.93×10^{-1}	5.21×10^{2}	7.20×10^{-4}	4.70×10^{2}	1.01×10^{-4}
0.2	7.33×10^{2}	9.33×10^{-2}	8.47×10^{2}	8.57×10^{-1}	5.77×10^{2}	1.77×10^{-3}	5.21×10^{2}	2.80×10^{-4}
0.25	9.07×10^{2}	3.52×10^{-1}	1.05×10^{3}	2.68×10^{0}	7.16×10^{2}	1.06×10^{-2}	6.48×10^{2}	2.10×10^{-3}
0.3	1.08×10^{3}	9.86×10^{-1}	1.24×10^{3}	6.64×10^{0}	8.53×10^{2}	4.12×10^{-2}	7.72×10^{2}	9.55×10^{-3}
0.35	1.25×10^{3}	2.27×10^{0}	1.43×10^{3}	1.40×10^{1}	9.91×10^{2}	1.21×10^{-1}	8.98×10^{2}	3.16×10^{-2}
0.4	1.41×10^{3}	4.58×10^{0}	1.61×10^{3}	2.65×10^{1}	1.12×10^{3}	2.92×10^{-1}	1.02×10^{3}	8.39×10^{-2}
0.45	1.57×10^{3}	8.39×10^{0}	1.80×10^{3}	4.60×10^{1}	1.25×10^{3}	6.13×10^{-1}	1.14×10^{3}	1.91×10^{-1}
0.5	1.73×10^{3}	1.43×10^{1}	1.97×10^{3}	7.47×10^{1}	1.38×10^{3}	1.16×10^{0}	1.26×10^{3}	3.85×10^{-1}
0.6	2.04×10^{3}	3.53×10^{1}	2.32×10^{3}	1.69×10^{2}	1.64×10^{3}	3.32×10^{0}	1.49×10^{3}	1.22×10^{0}
0.7	2.34×10^{3}	7.51×10^{1}	2.65×10^{3}	3.29×10^{2}	1.89×10^{3}	7.72×10^{0}	1.72×10^{3}	3.03×10^{0}
0.8	2.63×10^{3}	1.44×10^{2}	2.97×10^{3}	5.73×10^{2}	2.13×10^{3}	1.55×10^{1}	1.94×10^{3}	6.42×10^{0}
0.9	2.91×10^{3}	2.53×10^{2}	3.27×10^{3}	9.18×10^{2}	2.36×10^{3}	2.82×10^{1}	2.16×10^{3}	1.21×10^{1}
1	3.18×10^{3}	4.16×10^{2}	3.57×10^{3}	1.38×10^{3}	2.59×10^{3}	4.74×10^{1}	2.37×10^{3}	2.10×10^{1}
1.25	3.82×10^{3}	1.14×10^{3}	4.27×10^{3}	3.06×10^{3}	3.14×10^{3}	1.39×10^{2}	2.88×10^{3}	6.40×10^{1}
1.5	4.42×10^{3}	2.46×10^{3}	4.91×10^{3}	5.52×10^{3}	3.66×10^{3}	3.36×10^{2}	3.37×10^{3}	1.53×10^{2}
1.75	4.98×10^{3}	4.44×10^{3}	5.51×10^{3}	8.65×10^{3}	4.16×10^{3}	7.22×10^{2}	3.83×10^{3}	3.19×10^{2}
2	5.50×10^{3}	7.07×10^{3}	6.06×10^{3}	1.23×10^{4}	4.62×10^{3}	1.42×10^{3}	4.27×10^{3}	6.08×10^{2}
2.5	6.46×10^{3}	1.39×10^{4}	7.06×10^{3}	2.06×10^{4}	5.49×10^{3}	4.18×10^{3}	5.10×10^{3}	1.89×10^{3}
3	7.32×10^{3}	2.19×10^{4}	7.94×10^{3}	2.92×10^{4}	6.28×10^{3}	9.05×10^{3}	5.85×10^{3}	4.76×10^{3}
3.5	8.09×10^{3}	3.03×10^{4}	8.72×10^{3}	3.74×10^{4}	7.00×10^{3}	1.57×10^{4}	6.54×10^{3}	9.58×10^{3}
4	8.78×10^{3}	3.83×10^{4}	9.42×10^{3}	4.47×10^{4}	7.66×10^{3}	2.33×10^{4}	7.19×10^{3}	1.61×10^{4}
5	9.99×10^{3}	5.18×10^{4}	1.06×10^{4}	5.62×10^{4}	8.84×10^{3}	3.91×10^{4}	8.33×10^{3}	3.14×10^{4}
6	1.10×10^{3}	6.17×10^{4}	1.15×10^{4}	6.40×10^{4}	9.85×10^{3}	5.27×10^{4}	9.34×10^{3}	4.62×10^{4}
7	1.18×10^{4}	6.82×10^{4}	1.22×10^{4}	6.87×10^{4}	1.07×10^{4}	6.31×10^{4}	1.02×10^{4}	5.85×10^{4}
8	1.25×10^{4}	7.22×10^{4}	1.28×10^{4}	7.12×10^{4}	1.15×10^{4}	7.05×10^{4}	1.10×10^{4}	6.77×10^{4}
9	1.30×10^{4}	7.43×10^{4}	1.32×10^{4}	7.21×10^{4}	1.22×10^{4}	7.54×10^{4}	1.17×10^{4}	7.42×10^{4}
10	1.34×10^{4}	7.50×10^{4}	1.35×10^{4}	7.20×10^{4}	1.28×10^{4}	7.83×10^{4}	1.23×10^{4}	7.85×10^{4}

References

1. Malaney, R.A.; Mathews, G.J. Probing the Early Universe: A Review of Primordial Nucleosynthesis beyond the Standard Big Bang. *Phys. Rep.* **1993**, *229*, 145–219. [CrossRef]
2. Rauscher, T. *Essentials of Nucleosynthesis and Theoretical Nuclear Astrophysics*; IOP Publishing: Bristol, UK, 2020; ISBN 978-0-7503-1149-6.
3. Iliadis, C. *Nuclear Physics of Stars*, 2nd ed.; Wiley-VCH Verlag GmbH & Co. KGaA: Weinheim, Germany, 2015; ISBN 978-3-527-33648-7.
4. Romano, D. The Evolution of CNO Elements in Galaxies. *Astron. Astrophys. Rev.* **2022**, *30*, 7. [CrossRef]
5. Bertulani, C.A.; Shubhchintak. Primordial Nucleosynthesis with Non-Extensive Statistics. *Eur. Phys. J. Spec. Top.* **2024**, *233*, 2831–2842. [CrossRef]
6. Liu, N.; Gallino, R.; Cristallo, S.; Bisterzo, S.; Davis, A.M.; Trappitsch, R.; Nittler, L.R. New Constraints on the Major Neutron Source in Low-Mass AGB Stars. *Astrophys. J.* **2018**, *865*, 112. [CrossRef]
7. Lu, H.-L.; Li, Y.-B.; Luo, A.-L.; Zou, Z.-Q.; Kong, X.-M.; Yi, Z.-P.; Jones, H.R.A.; Liang, J.-C.; Li, S. A Review of the Search for AGB Stars. *Front. Astron. Space Sci.* **2025**, *12*, 1587415. [CrossRef]
8. Tsallis, C. Possible Generalization of Boltzmann-Gibbs Statistics. *J. Stat. Phys.* **1988**, *52*, 479–487. [CrossRef]
9. Csedreki, L.; Gyürky, G.; Rapagnani, D.; Ciani, G.F.; Aliotta, M.; Ananna, C.; Barbieri, L.; Barile, F.; Bemmerer, D.; Best, A.; et al. Status and Future Directions for Direct Cross-Section Measurements of the ^{13}C(α,n)^{16}O Reaction for Astrophysics. *J. Phys. G Nucl. Part. Phys.* **2024**, *51*, 105201. [CrossRef]

10. Battich, T.; Miller Bertolami, M.M.; Weiss, A.; Dorsch, M.; Serenelli, A.M.; Justham, S. The i-processes Nucleosynthesis during the Formation of He-Rich Hot-Subdwarf Stars. *Astron. Astrophys.* **2025**, *699*, A298. [CrossRef]
11. Prantzos, N. Production and Evolution of Li, Be, and B Isotopes in the Galaxy. *Astron. Astrophys.* **2012**, *542*, A67. [CrossRef]
12. Acharya, B.; Aliotta, M.; Balantekin, A.B.; Bemmerer, D.; Bertulani, C.A.; Best, A.; Brune, C.R.; Buompane, R.; Gialanella, L.; Cavanna, F.; et al. Solar Fusion III: New Data and Theory for Hydrogen-Burning Stars. *Rev. Mod. Phys.* **2025**, *97*, 035002. [CrossRef]
13. Wiescher, M. The History and Impact of the CNO Cycles in Nuclear Astrophysics. *Phys. Perspect.* **2018**, *20*, 124–158. [CrossRef]
14. Choplin, A.; Siess, L.; Goriely, S.; Martinet, S. Production of Lithium and Heavy Elements in AGB Stars Experiencing PIEs. *Galaxies* **2024**, *12*, 66. [CrossRef]
15. Kajino, T.; Mathews, G.J.; Fuller, G.M. Primordial Nucleosynthesis of Intermediate-Mass Elements in Baryon-Number-Inhomogeneous Big Bang Models–Observational Tests. *Astrophys. J.* **1990**, *364*, 7. [CrossRef] [PubMed]
16. Terasawa, M.; Sumiyoshi, K.; Kajino, T.; Mathews, G.J.; Tanihata, I. New Nuclear Reaction Flow during r-process Nucleosynthesis in Supernovae: Critical Role of Light, Neutron-Rich Nuclei. *Astrophys. J.* **2001**, *562*, 470–479. [CrossRef] [PubMed]
17. Igashira, M.; Ohsaki, T. Neutron Capture Nucleosynthesis in the Universe. *Sci. Technol. Adv. Mater.* **2004**, *5*, 567–573. [CrossRef]
18. Wiescher, M.; Görres, J.; Schatz, H. Break-out Reactions from the CNO Cycles. *J. Phys. G Nucl. Part. Phys.* **1999**, *25*, R133–R161. [CrossRef]
19. Beer, H.; Wiescher, M.; Kaeppeler, F.; Goerres, J.; Koehler, P.E. A Measurement of the $^{14}C(n,\gamma)^{15}C$ Cross Section at a Stellar Temperature of kT = 23.3 KeV. *Astrophys. J.* **1992**, *387*, 258. [CrossRef] [PubMed]
20. Horvath, A.; Weiner, J.; Galonsky, A.; Deak, F.; Higurashi, Y.; Ieki, K.; Iwata, Y.; Kiss, A.; Kolata, J.J.; Seres, Z.; et al. Cross Section for the Astrophysical $^{14}C(n,\gamma)^{15}C$ Reaction via the Inverse Reaction. *Astrophys. J.* **2002**, *570*, 926–933. [CrossRef]
21. Reifarth, R.; Heil, M.; Plag, R.; Besserer, U.; Dababneh, S.; Dörr, L.; Görres, J.; Haight, R.C.; Käppeler, F.; Mengoni, A.; et al. Stellar Neutron Capture Rates of ^{14}C. *Nucl. Phys. A* **2005**, *758*, 787–790. [CrossRef]
22. Reifarth, R.; Heil, M.; Forssén, C.; Besserer, U.; Couture, A.; Dababneh, S.; Dörr, L.; Görres, J.; Haight, R.C.; Käppeler, F.; et al. The $^{14}C(n,\gamma)$ Cross Section between 10 KeV and 1 MeV. *Phys. Rev. C* **2008**, *77*, 015804. [CrossRef]
23. Nakamura, T.; Fukuda, N.; Aoi, N.; Imai, N.; Ishihara, M.; Iwasaki, H.; Kobayashi, T.; Kubo, T.; Mengoni, A.; Motobayashi, T.; et al. Neutron Capture Cross Section of ^{14}C of Astrophysical Interest Studied by Coulomb Breakup of ^{15}C. *Phys. Rev. C* **2009**, *79*, 035805. [CrossRef]
24. Tkachenko, A.S.; Burkova, N.A.; Yeleusheva, B.M.; Dubovichenko, S.B. Estimation of the Effect of Tsallis Non-Extensive Statistics on the $^{14}C(n,\gamma)^{15}C$ Reaction Rate. *Front. Phys.* **2025**, *13*, 1688864. [CrossRef]
25. Jiang, Y.; He, Z.; Luo, Y.; Xin, W.; Chen, J.; Li, X.; Shen, Y.; Guo, B.; Li, G.; Pang, D.; et al. New Determination of the $^{14}C(n,\gamma)^{15}C$ Reaction Rate and Its Astrophysical Implications. *Astrophys. J.* **2025**, *989*, 231. [CrossRef]
26. Navratil, P.; Quaglioni, S.; Hupin, G.; Gennari, M.; Kravvaris, K. Halo Nuclei from Ab Initio Nuclear Theory. *Particles* **2026**, *9*, 57. [CrossRef]
27. Ma, T.; Guo, B.; Pang, D.; Li, Z.; Su, Y.; Li, X.; Shen, Y.; Wang, Y.; Li, Y.; Su, J.; et al. New Determination of Astrophysical $^{14}C(n,\gamma)^{15}C$ Reaction Rate from the Spectroscopic Factor of ^{15}C. *Sci. China Phys. Mech. Astron.* **2020**, *63*, 212021. [CrossRef]
28. Bhattacharyya, A.; Datta, U.; Rahaman, A.; Chakraborty, S.; Aumann, T.; Beceiro-Novo, S.; Boretzky, K.; Caesar, C.; Carlson, B.V.; Catford, W.N.; et al. Neutron Capture Cross Sections of Light Neutron-Rich Nuclei Relevant for r-process Nucleosynthesis. *Phys. Rev. C* **2021**, *104*, 045801. [CrossRef]
29. Görres, J.; Graff, S.; Wiescher, M.; Azuma, R.E.; Barnes, C.A.; Becker, H.W.; Wang, T.R. Proton Capture on ^{14}C and Its Astrophysical Implications. *Nucl. Phys. A* **1990**, *517*, 329–339. [CrossRef]
30. Iliadis, C.; Longland, R.; Champagne, A.E.; Coc, A.; Fitzgerald, R. Charged-Particle Thermonuclear Reaction Rates: II. Tables and Graphs of Reaction Rates and Probability Density Functions. *Nucl. Phys. A* **2010**, *841*, 31–250. [CrossRef]
31. Iliadis, C.; Longland, R.; Setoodehnia, K.; Marshall, C.; Mohr, P.; Psaltis, A. The 2025 Evaluation of Experimental Thermonuclear Reaction Rates (ETR25). *Astrophys. J. Suppl. Ser.* **2026**, *283*, 17. [CrossRef]
32. Wiescher, M.; Gorres, J.; Thielemann, F.-K. Capture Reactions on ^{14}C in Nonstandard Big Bang Nucleosynthesis. *Astrophys. J.* **1990**, *363*, 340. [CrossRef]
33. Kawano, L.H.; Fowler, W.A.; Kavanagh, R.W.; Malaney, R.A. Signatures of Inhomogeneity in the Early Universe. *Astrophys. J.* **1991**, *372*, 1. [CrossRef]
34. Shubhchintak; Neelam; Chatterjee, R. Capture Cross-Section and Rate of the $^{14}C(n,\gamma)^{15}C$ Reaction from the Coulomb Dissociation of ^{15}C. *Pramana J. Phys.* **2014**, *83*, 533–543. [CrossRef]
35. Dubovichenko, S.B. *Thermonuclear Processes in Stars and Universe*, 2nd ed.; Scholar's Press: Saarbrücken, Germany, 2015; ISBN 978-3-639-76478-9.
36. Dubovichenko, S.B. *Radiative Neutron Capture: Primordial Nucleosynthesis of the Universe*; De Gruyter: Berlin, Germany, 2019; ISBN 9783110619607.

37. Neudatchin, V.G.; Kukulin, V.I.; Pomerantsev, V.N.; Sakharuk, A.A. Generalized Potential-Model Description of Mutual Scattering of the Lightest p+d, d+^{3}He Nuclei and the Corresponding Photonuclear Reactions. *Phys. Rev. C* **1992**, *45*, 1512–1527. [CrossRef] [PubMed]
38. Kukulin, V.I.; Neudatchin, V.G.; Obukhovski, I.T.; Smirnov, Y.F. Clusters as Subsystems in Light Nuclei. In *Clusters as Subsystems in Light Nuclei*; Wildermuth, K., Kramer, P., Eds.; Vieweg+Teubner Verlag: Wiesbaden, Germany, 1983; pp. 1–155.
39. Dubovichenko, S.B.; Burkova, N.A.; Tkachenko, A.S.; Dzhazairov-Kakhramanov, A.V. Influence of Resonances on the ^{11}B(n,γ)^{12}B Reaction Rate. Capture to the Excited States of ^{12}B. *Int. J. Mod. Phys. E* **2023**, *32*, 2. [CrossRef]
40. Dubovichenko, S.B.; Dzhazairov-Kakhramanov, A.V. Thermonuclear Processes for Three Body System in the Potential Cluster Model. *Nucl. Phys. A* **2015**, *941*, 335–363. [CrossRef]
41. Sukhoruchkin, S.I.; Soroko, Z.N. *Exited Nuclear States. Supplement to I/25 A-E.*; Springer: Berlin/Heidelberg, Germany, 2016; ISBN 978-3-662-47801-1.
42. Ajzenberg-Selove, F. Energy Levels of Light Nuclei A = 13–15. *Nucl. Phys. A* **1991**, *523*, 1–196. [CrossRef]
43. Dubovichenko, S.B.; Kezerashvili, R.Y.; Burkova, N.A.; Dzhazairov-Kakhramanov, A.V.; Beisenov, B. Reanalysis of the ^{13}N(p,γ)^{14}O Reaction and Its Role in the Stellar CNO Cycle. *Phys. Rev. C* **2020**, *102*, 045805. [CrossRef]
44. Dubovichenko, S.B.; Tkachenko, A.S.; Kezerashvili, R.Y.; Burkova, N.A.; Dzhazairov-Kakhramanov, A.V. ^{6}Li(p,γ)^{7}Be Reaction Rate in the Light of the New Data of the Laboratory for Underground Nuclear Astrophysics. *Phys. Rev. C* **2022**, *105*, 065806. [CrossRef]
45. McCleskey, M.; Mukhamedzhanov, A.M.; Trache, L.; Tribble, R.E.; Banu, A.; Eremenko, V.; Goldberg, V.Z.; Lui, Y.-W.; McCleskey, E.; Roeder, B.T.; et al. Determination of the Asymptotic Normalization Coefficients for ^{14}C + n $\leftrightarrow$ ^{15}C, the ^{14}C(n,γ)^{15}C Reaction Rate, and Evaluation of a New Method to Determine Spectroscopic Factors. *Phys. Rev. C* **2014**, *89*, 044605. [CrossRef]
46. Moschini, L.; Yang, J.; Capel, P. ^{15}C: From Halo Effective Field Theory Structure to the Study of Transfer, Breakup, and Radiative-Capture Reactions. *Phys. Rev. C* **2019**, *100*, 044615. [CrossRef]
47. Hebborn, C.; Capel, P. Halo Effective Field Theory Analysis of One-Neutron Knockout Reactions of ^{11}Be and ^{15}C. *Phys. Rev. C* **2021**, *104*, 024616. [CrossRef]
48. Mukhamedzhanov, A.M.; Burjan, V.; Gulino, M.; Hons, Z.; Kroha, V.; McCleskey, M.; Mrázek, J.; Nguyen, N.; Nunes, F.M.; Piskoř, Š.; et al. Asymptotic Normalization Coefficients from the ^{14}C(d,p)^{15}C Reaction. *Phys. Rev. C* **2011**, *84*, 024616. [CrossRef]
49. Herndl, H.; Hofinger, R.; Jank, J.; Oberhummer, H.; Görres, J.; Wiescher, M.; Thielemann, F.-K.K.; Brown, B.A. Reaction Rates for Neutron Capture Reactions to C, N, and O Isotopes to the Neutron Rich Side of Stability. *Phys. Rev. C* **1999**, *60*, 064614. [CrossRef]
50. Pramanik, U.D.; LAND-CB-FRS-Collaboration, L.-C.-F.-C. Structure and Reaction Studies of Loosely Bound Nuclei Using Radioactive Nuclear Beams. *Prog. Theor. Phys. Suppl.* **2002**, *146*, 427–431. [CrossRef]
51. Timofeyuk, N.K.; Baye, D.; Descouvemont, P.; Kamouni, R.; Thompson, I.J. ^{15}C–^{15}F Charge Symmetry and the ^{14}C(n,γ)^{15}C Reaction Puzzle. *Phys. Rev. Lett.* **2006**, *96*, 162501. [CrossRef] [PubMed]
52. Summers, N.C.; Nunes, F.M. Extracting (n,γ) Direct Capture Cross Sections from Coulomb Dissociation: Application to ^{14}C(n,γ)^{15}C. *Phys. Rev. C* **2008**, *78*, 011601. [CrossRef]
53. Esbensen, H.; Reifarth, R. Erratum: Coulomb Dissociation of ^{15}C and Radiative Neutron Capture on ^{14}C [Phys. Rev. C 80, 024608 (2009)]. *Phys. Rev. C* **2009**, *80*, 059904. [CrossRef]
54. Capel, P.; Nollet, Y. Reconciling Coulomb Breakup and Neutron Radiative Capture. *Phys. Rev. C* **2017**, *96*, 015801. [CrossRef]
55. Kim, K.; Kim, Y.; He, Z.; Choi, Y.; Luo, Y.; Kajino, T.; Tanihata, I.; Diehl, R. Impact of Light-Mass Nuclear Reactions on the r-process Nucleosynthesis, Revisited. *Astrophys. J.* **2026**, *998*, 253. [CrossRef]
56. Zhang, L.-Y.; He, J.-J.; Kusakabe, M.; He, Z.-Y.; Kajino, T. Thermonuclear ^{17}O(n,γ)^{18}O Reaction Rate and Its Astrophysical Implications. *Astrophys. J.* **2022**, *927*, 92. [CrossRef]
57. Dubovichenko, S.B.; Uzikov, Y.N. Astrophysical S Factors of Reactions with Light Nuclei. *Phys. Part. Nucl.* **2011**, *42*, 251–301. [CrossRef]
58. Dubovichenko, S.; Burtebaev, N.; Dzhazairov-Kakhramanov, A.; Alimov, D. Astrophysical S-Factor of the Radiative Proton Capture on ^{14}C at Low Energies. *Mod. Phys. Lett. A* **2014**, *29*, 1450125. [CrossRef]
59. Nassurlla, M.; Burtebayev, N.; Sakuta, S.B.; Nassurlla, M.; Sabidolda, A.; Artemov, S.V.; Ruziev, E.T.; Ergashev, F.K.; Tojiboev, O.R.; Rusek, K.; et al. ^{11}B(^{15}N,^{14}C)^{12}C Reaction Mechanisms and ANC for the ^{15}N $\rightarrow$ ^{14}C + p Configuration. *Acta Phys. Pol. B Proc. Suppl.* **2023**, *16*, 1. [CrossRef]
60. Ruziev, E.T.; Artemov, S.V.; Tojiboev, O.R. ANC and SF of Bound States in ^{15}N$\rightarrow$^{14}C+p, ^{16}O$\rightarrow$^{15}N+p, ^{19}F$\rightarrow$^{18}O+p, ^{32}S$\rightarrow$^{31}P+p. *Int. J. Mod. Phys. E* **2024**, *33*, 6. [CrossRef]
61. Dubovichenko, S.B.; Dzhazairov-Kakhramanov, A.V. Phase Shift Analysis of p^{14}C Scattering at the Energy of the $^{2}S_{1/2}$ Resonance. *Russ. Phys. J.* **2016**, *58*, 1258–1264. [CrossRef]
62. Nuclear Reaction Database (EXFOR). Available online: http://cdfe.sinp.msu.ru/exfor/index.php (accessed on 23 June 2026).
63. Li, Y.J.; Li, Z.H.; Li, E.T.; Bai, X.X.; Su, J.; Guo, B.; Wang, B.X.; Yan, S.Q.; Zeng, S.; Li, Z.C.; et al. New Determination of the Astrophysical ^{13}C(p,γ)^{14}N S(E) Factors and Reaction Rates via the ^{13}C(^{7}Li,^{6}He)^{14}N Reaction. *Eur. Phys. J. A* **2012**, *48*, 13. [CrossRef]

64. Dubovichenko, S.B.; Tkachenko, A.S.; Kezerashvili, R.Y.; Burkova, N.A.; Yeleusheva, B.M. Astrophysical S-Factor and Reaction Rate for $^{15}N(p,\gamma)^{16}O$ within the Modified Potential Cluster Model. *Chin. Phys. C* **2024**, *48*, 044104. [CrossRef]
65. Szücs, T.; Mohr, P. Determination of γ-Ray Widths in ^{15}N Using Nuclear Resonance Fluorescence. *Phys. Rev. C* **2015**, *92*, 044328. [CrossRef]
66. Descouvemont, P. Microscopic Cluster Study of the C Isotopes. *Nucl. Phys. A* **2000**, *675*, 559–571. [CrossRef]
67. Hou, S.Q.; He, J.J.; Parikh, A.; Daid, K.; Bertulani, C. Big-Bang Nucleosynthesis Verifies Classical Maxwell-Boltzmann Distribution. *arXiv* **2014**. [CrossRef]
68. Hou, S.Q.; He, J.J.; Parikh, A.; Kahl, D.; Bertulani, C.A.; Kajino, T.; Mathews, G.J.; Zhao, G. Non-Extensive Statistics to the Cosmological Lithium Problem. *Astrophys. J.* **2017**, *834*, 165. [CrossRef]
69. Navas, S.; Amsler, C.; Gutsche, T.; Hanhart, C.; Hernández-Rey, J.J.; Lourenço, C.; Masoni, A.; Mikhasenko, M.; Mitchell, R.E.; Patrignani, C.; et al. Review of Particle Physics. *Phys. Rev. D* **2024**, *110*, 030001. [CrossRef]
70. Chart of Nucleus Shape and Size Parameters. Available online: http://cdfe.sinp.msu.ru/cgi-bin/muh/radcard.cgi?z=3&a=9&td=123456 (accessed on 23 June 2026).
71. Audi, G.; Wapstra, A.H. The 1995 Update to the Atomic Mass Evaluation. *Nucl. Phys. A* **1995**, *595*, 409–480. [CrossRef]
72. Liatard, E.; Bruandet, J.F.; Glasser, F.; Kox, S.; Chan, T.U.; Costa, G.J.; Heitz, C.; El Masri, Y.; Hanappe, F.; Bimbot, R.; et al. Matter Distribution in Neutron-Rich Light Nuclei and Total Reaction Cross-Section. *Europhys. Lett.* **1990**, *13*, 401–404. [CrossRef]
73. Wang, J.S.; Shen, W.Q.; Zhu, Z.Y.; Feng, J.; Guo, Z.Y.; Zhan, W.L.; Xiao, G.Q.; Cai, X.Z.; Fang, D.Q.; Zhang, H.Y.; et al. RMF Calculation and Phenomenological Formulas for the RMS Radii of Light Nuclei. *Nucl. Phys. A* **2001**, *691*, 618–630. [CrossRef]
74. Ozawa, A.; Suzuki, T.; Tanihata, I. Nuclear Size and Related Topics. *Nucl. Phys. A* **2001**, *693*, 32–62. [CrossRef]
75. Ozawa, A.; Bochkarev, O.; Chulkov, L.; Cortina, D.; Geissel, H.; Hellström, M.; Ivanov, M.; Janik, R.; Kimura, K.; Kobayashi, T.; et al. Measurements of Interaction Cross Sections for Light Neutron-Rich Nuclei at Relativistic Energies and Determination of Effective Matter Radii. *Nucl. Phys. A* **2001**, *691*, 599–617. [CrossRef]
76. Kanungo, R.; Horiuchi, W.; Hagen, G.; Jansen, G.R.; Navratil, P.; Ameil, F.; Atkinson, J.; Ayyad, Y.; Cortina-Gil, D.; Dillmann, I.; et al. Proton Distribution Radii of $^{12\text{-}19}C$ Illuminate Features of Neutron Halos. *Phys. Rev. Lett.* **2016**, *117*, 102501. [CrossRef] [PubMed]
77. Ahmad, S.; Usmani, A.A.; Khan, Z.A. Matter Radii of Light Proton-Rich and Neutron-Rich Nuclear Isotopes. *Phys. Rev. C* **2017**, *96*, 064602. [CrossRef]
78. Dobrovolsky, A.V.; Korolev, G.A.; Tang, S.; Alkhazov, G.D.; Colò, G.; Dillmann, I.; Egelhof, P.; Estradé, A.; Farinon, F.; Geissel, H.; et al. Nuclear Matter Distributions in the Neutron-Rich Carbon Isotopes $^{14-17}C$ from Intermediate-Energy Proton Elastic Scattering in Inverse Kinematics. *Nucl. Phys. A* **2021**, *1008*, 122154. [CrossRef]
79. Rahi, S.A.; Flaiyh, G.N. Study of Matter Density Distributions, Elastic Electron Scattering Form Factors and Root Mean Square Radii of ^{9}C, ^{12}N, ^{23}Al, ^{11}Be and ^{15}C Exotic Nuclei. *Iraqi J. Sci.* **2022**, *63*, 1018–1029. [CrossRef]
80. Mouadil, M.; Khouaja, A.; Jdair, O.; Elabssaoui, Y.; Bouhssa, M.L.; Badane, H.; Mhalli, I.; Sobhy, Z.; Hasbi, L.; Elouardi, B.; et al. Matter Distribution of $^{12\text{-}20,22}C$ Isotopes. *Phys. Rev. C* **2024**, *109*, 054330. [CrossRef]
81. Li, L.Y.; Tu, X.L.; Zhang, J.T.; Zhang, G.Q. Nuclear Matter Distribution Radius Compilation and Evaluation: NMRCE2025. *At. Data Nucl. Data Tables* **2025**, *166*, 101747. [CrossRef]
82. Ozawa, A.; Tanihata, I.; Kobayashi, T.; Sugahara, Y.; Yamakawa, O.; Omata, K.; Sugimoto, K.; Olson, D.; Christie, W.; Wieman, H. Interaction Cross Sections and Radii of Light Nuclei. *Nucl. Phys. A* **1996**, *608*, 63–76. [CrossRef]
83. Abdullah, S.Q.; Abdullah, A.N. Matter Density Distributions and Reaction Cross Sections for ^{8}Li and ^{22}N Exotic Nuclei. *Iraqi J. Sci.* **2022**, *63*, 1030–1038. [CrossRef]
84. Yamaguchi, T.; Hachiuma, I.; Kitagawa, A.; Namihira, K.; Sato, S.; Suzuki, T.; Tanihata, I.; Fukuda, M. Scaling of Charge-Changing Interaction Cross Sections and Point-Proton Radii of Neutron-Rich Carbon Isotopes. *Phys. Rev. Lett.* **2011**, *107*, 032502. [CrossRef] [PubMed]
85. Zhao, J.W.; Sun, B.-H.; Tanihata, I.; Terashima, S.; Prochazka, A.; Xu, J.Y.; Zhu, L.H.; Meng, J.; Su, J.; Zhang, K.Y.; et al. Isospin-Dependence of the Charge-Changing Cross-Section Shaped by the Charged-Particle Evaporation Process. *Phys. Lett. B* **2023**, *847*, 138269. [CrossRef]
86. Zhao, J.W.; Sun, B.-H.; Tanihata, I.; Xu, J.Y.; Zhang, K.Y.; Prochazka, A.; Zhu, L.H.; Terashima, S.; Meng, J.; He, L.C.; et al. Charge Radii of $^{11-16}C$, $^{13-17}N$ and $^{15-18}O$ Determined from Their Charge-Changing Cross-Sections and the Mirror-Difference Charge Radii. *Phys. Lett. B* **2024**, *858*, 139082. [CrossRef]

Disclaimer/Publisher's Note: The statements, opinions and data contained in all publications are solely those of the individual author(s) and contributor(s) and not of MDPI and/or the editor(s). MDPI and/or the editor(s) disclaim responsibility for any injury to people or property resulting from any ideas, methods, instructions or products referred to in the content.